

## 国際化推進共同研究概要

No.13

タイトル: Mechanical properties of FRP ply splice structures.

研究代表者: CHEN, Dingding

所内世話人: 新川 和夫

実施期間: 年月日～月日日

概要: 繊維強化複合材料で構造物が大型化すると、2つ以上の部品を接合することにより要求される寸法の構造物を作製することとなる。本研究では繊維強化複合材料の接合部の力学的特性を評価するために、炭素繊維強化複合材料(CFRP)接合部の引張り試験を行った。試験片として、CFRP積層間隔を(i)4cmとした場合、(ii)2.6cmとした場合、(iii)試験片(ii)の外部に8cmのCFRPをカバーした3種類を作製した。その結果、引張り強度が試験片(i)と(ii)で差が生じないこと、試験片(iii)で大きく増加することを明らかにした。

## TENSILE PROPERTIES OF FRP PLY SPLICE STRUCTURES

Dingding Chen<sup>1</sup>, Manyi Wang<sup>1</sup>, Yueyao Shen<sup>2</sup> and Kazuo Arakawa<sup>3</sup>

<sup>1</sup> College of Basic Education, National University of Defense Technology, China.

**Keywords:** fiber reinforced composites, Ply splice, Tensile property

### ABSTRACT

When the FRP structure becomes large, it is required to splice two or more plies to meet the size requirement. In order to understand the mechanical property of the FRP ply splice structure and get strong ply splice structures, the tensile properties of three kinds of unidirectional CFRP ply splice structures have been tested in the previous work in [1]. In this paper, another two structures were designed based on the S1 structure in [1], in order to improve the strength of this type of the ply splice structure. Compared with the S1 structure, the difference of the S1-1 structure was that the spliced point of each ply was optimized to extend the distance between the nearest spliced points. In the S1-2 structure, additional two carbon fiber fabrics were attached on each side of the S1-1 structure to restrain the bending of the specimen under a tensile load to improve the tensile strength. The results show that there is no big difference of the tensile strength between S1 and S1-1 structures, however, S1-2 really performs much higher tensile strength.

### 1 INTRODUCTION

Due to high strength and low density, fiber reinforced plastics (FRP) have been used widely, and FRP structures with large size are required by more and more applications. When the FRP structure becomes large, only one reinforcement ply may not large enough. In the previous work [1], the tensile properties of three kinds of unidirectional CFRP ply splice structures were studied. The results show that, inducing ply splices into CFRP materials, the tensile strength decreases evidently. Due to the ply splice, stress concentrations occur, and the initial fracture happens in the ply splice position, leading to the final fracture on the interfaces between different plies. The interlaminar shear stress and the tensile stress in the through-thickness direction near the ply splice position are the key factors leading to the initial failure. In this paper, some improvements were made based on one of the three ply splice structures, expecting to get higher strength.

### 2 EXPERIMENTS

Two kinds of CFRP plates with ply splice structures were made through vacuum assisted resin transfer molding (VaRTM) process. As shown in Figure 1, the black line represents the unidirectional carbon fiber fabric, TENAX STS from Saeertex GmbH. The matrix was XNR/H6815 epoxy resin from Nagase. Four fabrics were adopted in each kind of specimens. The thickness of all the specimens is about 2 mm. The fiber volume content is about 55%.

The S1 specimen is the structure in [1]. S1-1 was modified from S1. The splice points on the first and the fourth ply were changed, in order to extend the distance between the splice points on the first (or the second) and the third ply (or the fourth). Based on S1-1, additional two carbon fiber fabrics were attached on each side of it, getting S1-2 specimens.

Static tensile tests were performed to evaluate the four joints. The dimensions of the specimens are shown in Figure 2; the length was 250 mm and the width was 10 mm. Two pairs of tabs made with glass fibre-reinforced plastic (GFRP) were used for each specimen to reduce stress concentrations. The length of the tab was 50 mm. The crosshead speed was 1 mm/min. The tensile stress was along the fibre direction. At least four samples were tested to get the average tensile strength.

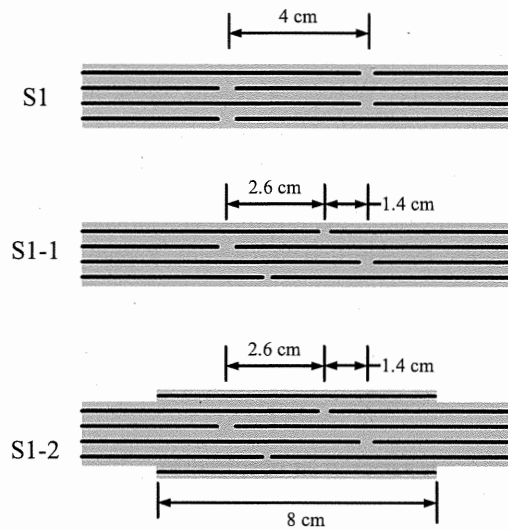


Figure 1: Sketch of the three ply splice structures

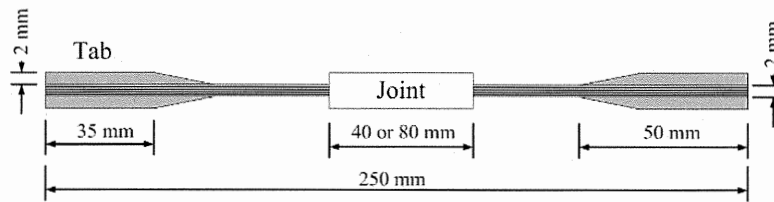


Figure 2: Dimensions of specimens used for tensile strength testing.

### 3 RESULTS AND DISCUSSION

The tensile strength of the structures is shown in Figure 3. The strength of S1-1 structure was 14.2 kN with a standard deviation of 0.57 kN, which was similar with S1 structure. Compared with S1 structure, the strength of S1-2 increased by 21% to 17.4 kN which was about half the strength of the CFRP specimen. The standard deviation was 0.88 kN. Figure 4 shows the typical load-displacement curves for a S1-1 and a S1-2 specimen, exhibiting brittle properties. Figure 5 and 6 show the classical fracture evolution of a S1-1 and a S1-2 structures. For the S1-1 specimen, the initiation fracture happened at about 80.1s, counting from the start of the tension. The initiation fracture of the S1-2 specimen occurred much later, at about 102s.

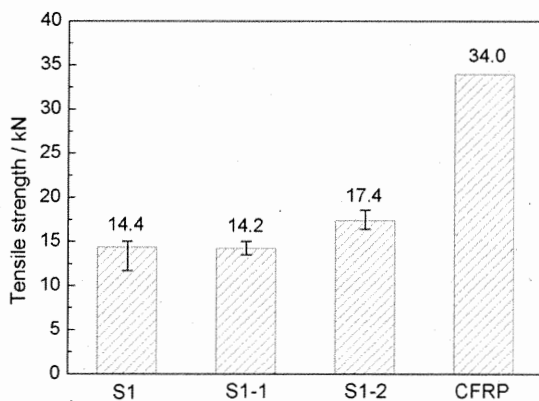


Figure 3. Tensile strength of different ply splice structures and CFRP plate for 10 mm wide specimens

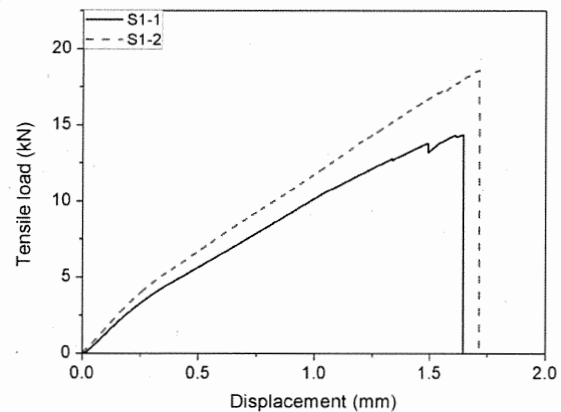


Figure 4. Typical load-displacement curves for a S1-1 and a S1-2 specimen.

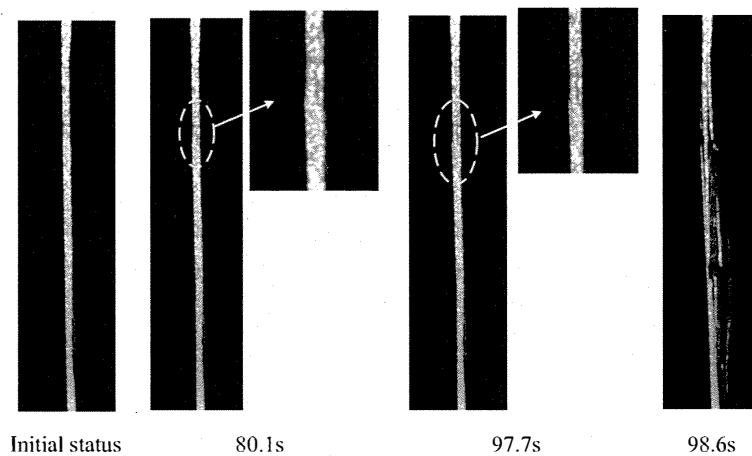


Figure 5. Fracture evolution of S1-1 structure

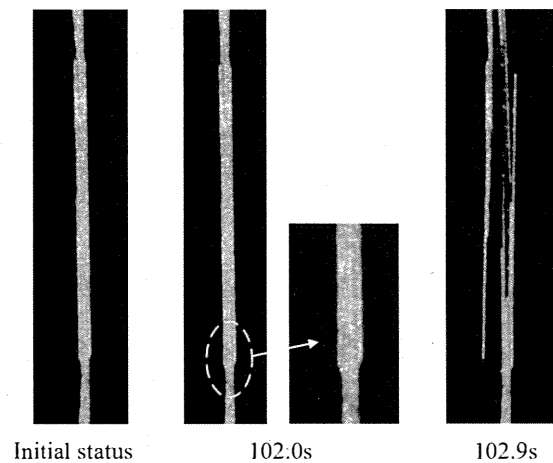


Figure 6. Fracture evolution of S1-2 structure

Compared with the S1 structure, the difference of S1-1 structure is that the spliced point of each ply is optimized to extend the distance between the nearest spliced points. This modification may have obvious positive effect on reducing the fiber direction tensile stress component of the stress concentration in the vicinity of the spliced point, however, have almost no effect on the other components. The previous work has shown that the tensile stress along the fiber direction is not the key factor deciding the final strength, coinciding with the strength of the S1-1 structure. In the S1-2 structure, additional two carbon fiber fabrics were attached on each side of S1-1 structure to restrain the bending of the specimen under a tensile load to improve the tensile strength. The results show that this modification really can make the structure stronger.

#### 4 CONCLUSIONS

In this paper, two structures were designed based on the S1 structure in [1] in order to improve the strength of this type of the ply splice structure. Compared with the S1 structure, the difference of S1-1 structure was that the spliced point of each ply was optimized to extend the distance between the nearest spliced points. In S1-2 structure, additional two carbon fiber fabrics were attached on each side of S1-1 structure to restrain the bending of the specimen under a tensile load to improve the tensile strength. The results show that there is no big difference of the tensile strength between S1 and S1-1 structures, however, S1-2 really performs much higher tensile strength, coinciding with the analysis and conclusions in [1].

### **ACKNOWLEDGEMENTS**

This work was supported by the Natural Science Foundation of China (NSFC) [grant numbers 51503223] and the Collaborative Research Program of the Research Institute for Applied Mechanics, Kyushu University.

### **REFERENCES**

- [1] D. Chen, M. Wang, K. Arakawa, S. Jiang, K. Wu and Q. Hu, Tensile properties of FRP ply splice structures, *Acta Materiae Compositae Sinica*, pp. 1-6.

## 国際化推進共同研究概要

No.14

タイトル: Effects of loading direction and microstructure on bending strength of CFRP laminates fabricated by vacuum-assisted RTM

研究代表者: CHOI, Nak-Sam

所内世話人: 新川 和夫

概要: 接合部を有する炭素繊維強化複合材料(CFRP)を真空樹脂含浸法を応用することにより作製した。接合法として縫製法および多層接合法を用いてCFRP試験片を作製し、曲げ計測により強度評価を行った。縫製法および多層接合法を適応することにより、CFRP接合部の曲げ強度が大きく増加することを解明した。

# Bending strength of CFRP laminated adhesive joints fabricated by vacuum-assisted resin transfer molding

Mahmoud R. Abusrea<sup>a,b</sup>, Seung-Wook Han<sup>c</sup>, Kazuo Arakawa<sup>d</sup>, Nak-Sam Choi<sup>e\*</sup>

<sup>a</sup> Faculty of Engineering, Cairo University, Giza 12613, Egypt

<sup>b</sup> Interdisciplinary Graduate School of Engineering Sciences, Kyushu University, Fukuoka 816-8580, Japan

<sup>c</sup> Department of Mechanical Engineering, Hanyang University, Ansan 426-791, South Korea

<sup>d</sup> Research Institute for Applied Mechanics, Kyushu University, Fukuoka 816-8580, Japan

## Abstract

The laminated joints in this work were an adhesive joint constructed using two dry carbon fiber halves. For the joints, some improvements were introduced to enhance the bending strength performance: Stitching of the two halves together by fiber bundles, and inserting extra carbon fiber covers in the joint connection. We studied three adhesive joints: conventional basic laminated joint and the two improved laminated joints. All joint specimens were fabricated in our laboratory using vacuum-assisted resin transfer molding (VARTM) process. The joint performance was evaluated with a bending test, and was compared to the bending strength of jointless carbon fiber reinforced plastic (CFRP) laminate. Two acoustic emission (AE) sensors were placed on a specimen to monitor the fracture progresses during the test. The improved laminated joints, stitched joint and multiple-covers-overlapped joint, showed enhanced bending strength and joint efficiency as well. The improvement depended significantly on the number of carbon fiber layers. The maximum increase in comparison to the jointless CFRP was 24% for stitched laminated joint of 5 layer laminates and 58% for multiple-overlapped joint of 6 layer laminates, respectively. Such high joint efficiency was due to carbon fiber reinforcement effects in the joints that many carbon fibers supported the strength in advance of reaching the maximum load point as indicated by AE detection analysis.

**Keywords**— CFRP joints, vacuum-assisted resin transfer molding, bending strength, joint efficiency

## 1. Introduction

The use of carbon fiber reinforced plastic (CFRP) composites in engineering structures has many advantages because of their high mechanical performances such as high strength-to-weight and stiffness-to-weight ratios [1]. For this reason, they have applied to heavy duty structures in aviation, space [2, 4], automotive [3], shipbuilding [4], and wind turbine [5]. These applications generally involve large-scale manufacturing, and the parts are made from smaller components and are joined together. In this case the mechanical performance of such CFRP structures is highly dependent on the properties of the joint parts.

Since composite joints work as crucial load-carrying elements their design and analysis is a key process in the large-scale applications to accomplish light weight, low-cost and efficient composite structure integration [6]. There are conventional mechanical fasteners such as bolts, pins, and rivets to join CFRP structures [7]. These mechanical joints are often preferred due to the conveniences that such fastening joints can be disassembled for repair and/or recycling [8]. However, drilling holes made for parts joining may induce localized damage in the composite due to stress concentration when the joint is loaded. In contrast, adhesively bonded joints may have mechanical advantages better than bolted joints because the reinforcing fibers are not cut, and thus the stresses are transmitted more homogeneously [9]. Besides, bonded joints can provide good structural integrity, low weight and high strength-to-weight ratios [10-12].

Nowadays adhesive composite joints are applied widely in many composite structures for aerospace, turbine, and ship designs [13]. These engineering structures are subjected to combinations of static, fatigue and impact loadings. Not only conventional single-lap [9], double-lap [14] and stepped [15] adhesive joints, but also improved adhesive joints have been studied to improve the mechanical performance of adhesive composite joints. For instance, Lobel et al. [16] enhanced tensile strength by introducing z-pinning into CFRP double-lap joints. Another approach for adhesive joint improvement was reported by Mouritz et al. [17] who placed spiked metal sheets in the bond-line to facilitate mechanical load transfer. Furthermore, stitching was a technique for reinforcing the laminated joint. Dransfield et al. [18] and Heß et al. [19] clarified that the stitching enhanced the fracture toughness of laminated composites under peel loading. Kim et al. [20] made some stepped-lap joints as a function of the number of steps, joint length, and edge angle of the adherends, and showed a considerable improvement in the fatigue performance by increasing the number of steps

and the edge angle.

Vacuum-assisted resin transfer molding (VARTM) has been recognized as a useful fabrication technique to make large-scale CFRP structures containing adhesive joints [19-20]. We developed the technique in our laboratory to apply to the fabrication of wind-lens parts for offshore wind power applications [10-12]. Using this VARTM technique several novel adhesive bonded joint structures were fabricated on the basis of stacking the carbon fiber layers to evaluate their tensile strength performances: The first type joints were constructed from partially un-moulded dry carbon-fabric layers [12]. Tensile testing indicated that the novel double-lap joints were more than twice as strong as a classical double-lap joint. The second type joints were made from two pairs [10]: one pair was two mating dry carbon fibers, and the other pair was dry carbon and pre-molded CFRP fabrics. The laminated adhesive joint from two dry carbon fibers achieved a higher tensile strength than the corresponding other pair joint. Multi-overlapped joint showed the best excellence equivalent to 85% of the tensile strength of the jointless CFRP. Furthermore a stitching was applied to the above joints [11]: the stitching improved the tensile strength of the former joints constructed of two dry carbon fibers, whereas it decreased the tensile strength of the latter joints. The novel adhesive joints have been evaluated only in terms of tensile strength. In real working situations the adhesive joint structures are commonly subjected to bending moments caused by a strong wind power, and thus their bending performances need to be extensively investigated as an important aspect.

In this study, a CFRP laminated adhesive joint indicating a basic laminated joint (BLJ) is fabricated using the VARTM as schematically illustrated in Fig.1. This joint is constructed of two mated dry carbon fiber halves. Two modifications are introduced to the joint. One is application of a stitching to the basic laminated adhesive joint (i.e., a stitched laminated joint, SLJ) and the other is addition of carbon fiber covers onto the conventional adhesive joint (i.e., a multiple-covers laminated joint, MCLJ). The three types of joint specimens are cured and then subjected to three-point bending tests with acoustic emission (AE) measurement. The performances of adhesive joints are characterized in terms of bending strength in comparison to the jointless CFRP laminates. The objective of this work is to accomplish improved bending strength in the joint types. Important fracture mechanisms of the joints are clarified by detection of AE measurement data in combination with optical and scanning electron microscopy.

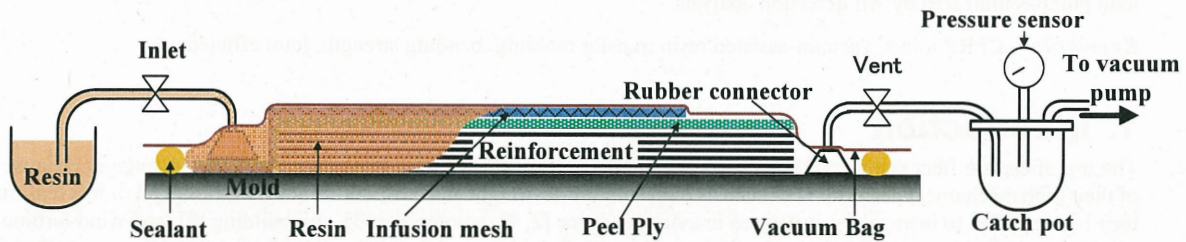


Figure 1. Schematic diagram of the vacuum-assisted resin transfer molding (VARTM) process

## 2. Experimental method

### 2.1. Materials and Fabrication

The composites and adhesive joints consisted of carbon fabric shown in Table 1 and a resin (Denatite XNR/H 6815, supplied by Nagase & Co.). The resin was a mixture of XNR6815 and XNH6815 at a weight ratio of 100:27. The viscosity of the resin mixture at 25°C was 260 MPa·s prior to the resin infusion in VARTM process.

Table 1. Detailed information of the carbon fabric [30]

Carbon fiber designation	Style	No. of filaments	Weight	Density	Thickness	Tensile strength	Tensile modulus	Elongation
			g/m <sup>2</sup>	g/cm <sup>3</sup>	mm	MPa	GPa	%
TRK976PQ RW	UD 1M	12,000	317	1.82	0.33	4,900	253	1.9

The laminated joints proposed in this work are a composite adhesive joint constructed of two mating dry carbon halves which were stacked in a pre-determined order prior to the VARTM process [10-12] schematically shown in Fig.1. Three joint types were adopted in this work. The adhesive joint constructed of only two mating dry carbon halves was a basic original type (see BLJ of Fig. 2a). The joint length was 40 mm in the total specimen length of 80 mm. The fiber volume fraction measured for the joints was approximately 62%. One improvement to this joint was made by applying a stitching technique. Fig. 2b shows a stitched laminate joint (SLJ). We conducted stitching with carbon bundles of the same carbon fiber type, which were applied perpendicular to the plane of the laminate [18-19]. Abusrea and Arakawa [11] showed a weakened stepped joint in which stitching was applied; the tensile strength of the stitched stepped joint was 26% lower. However, it showed improved tensile strength when the stitching was applied to the dry carbon-to-dry carbon joint state. The other improvement was made by adding carbon fiber covers of 40 mm in length which had been prepared beforehand by sectioning the carbon fiber layers. Each carbon fiber cover was put on the contact region between the end parts of two mating dry carbon fiber layers. After finishing the VARTM process [10,11] the inserted carbon fiber covers may reinforce the interphase layer between the two overlapping carbon halves, and may alleviate stress concentration at the fiber ends of carbon halves. This joint type is named as a multiple-covers-overlapped laminate joint (MCLJ) (see Fig. 2c). We applied four different numbers of carbon fiber layers for all joints. We chose 5, 6, 7 and 10 carbon fiber layers as these numbers were common in industry use. On the other hand for the basic type of a laminated joint, two different cases were made: a normal BLJ and a 'shifted' basic laminated joint (S-BLJ). For the normal BLJ, the six and ten carbon fiber layers were stacked 'correctly' at their right positions; that is, there was no gap between the fiber ends (Fig. 2a). For S-BLJ, the five and seven carbon fiber layers were a bit shifted to form a gap between the fiber ends (Fig. 2b). Because a shifted placement of carbon fiber layer may be conducted during mold preparation for this kind of adhesive joint fabrication, the S-BLJ was used to examine the effects of such shifting on the final product quality in terms of thickness variation, and on the mechanical performance in terms of bending strength.

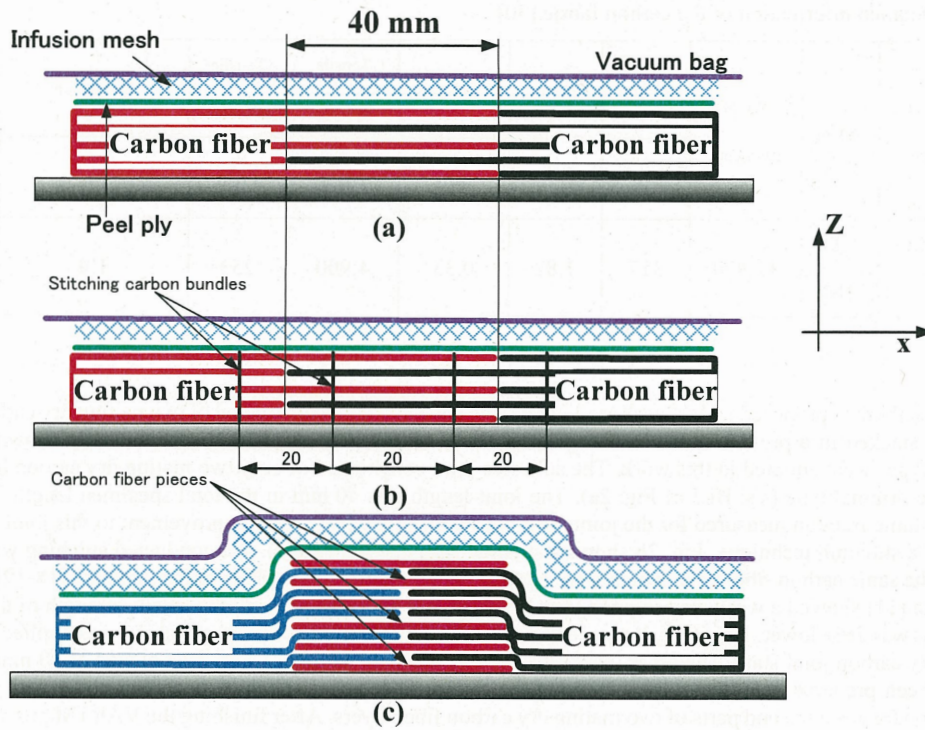


Figure 2. (a) Basic laminated joint (BLJ). (b) Stitched laminated joint (SLJ). (c) Multiple-cover laminated joint (MCLJ)

All CFRP fabrics and joints were fabricated using the VARTM process shown in Fig. 1. Composite joint fabrication with the VARTM involved three steps: mold preparation, filling with resin, and curing. In the beginning step the mold surface was treated with a mold release agent (TR High-Temp). The dry carbon fiber layers were stacked on the mold according to the desired joint types. The stacked carbon fiber layers were covered by a peel ply. Both the chemical agent and peel ply were applied so that the final composite joints could be released readily after curing. Then an infusion mesh was applied over the peel ply, providing two main functions: promoting resin flow and facilitating the drawing of resin into any voids before resin curing. Two rubber connectors and spiral tube pieces were placed as the inlet for infusion and the vent for air and excess resin elimination, respectively. The whole package was enclosed in a vacuum bag and tightly sealed with gum tape sealant. Finally, two external hoses were connected to the inlet and vent. One was connected to the resin source and the other to a vacuum pump. To ensure a leakage-free mold, a sealing test was performed in accordance with an appropriate procedure before resin filling. After the resin filled the stacked fiber joint reinforcements on the mold and excessive resin exited the vent, the inlet was closed and the vent was left open for 24 h until the resin cured. All VARTM processes were performed at room temperature. Details of the VARTM process is explained in the previous papers [10, 11].

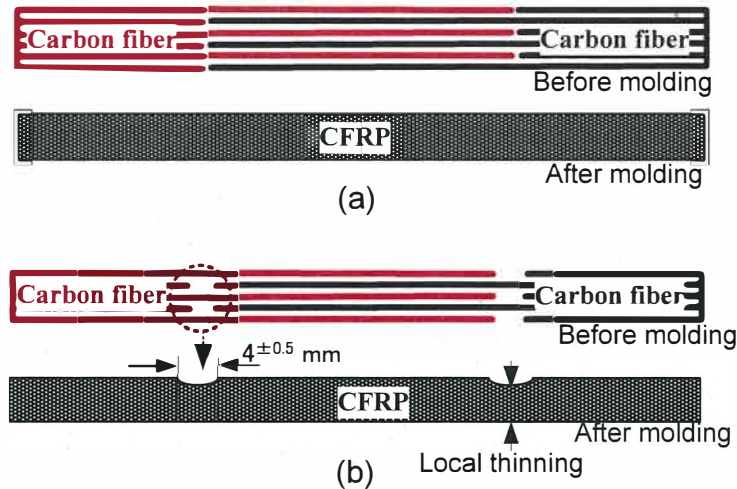


Figure 3. Schematic drawing before and after molding for the (a) normal basic laminated joint (BLJ) and (b) shifted laminated joint (S-BLJ).

## 2.2. Mechanical testing with AE measurement

The nominal bending strength was measured [24] to evaluate the joints' mechanical performances. The cured CFRP joints were sectioned to form specimens for the three-point bending tests, with the geometry shown in Fig. 4. Five specimens were prepared for each test condition. The span ( $L$ ) and the width ( $W$ ) of the test specimens were 50mm and 12.7mm, respectively. The thickness ( $t$ ) of the joints was varied according to the joint types of Fig.1, and thus measured for the individual joint type in advance of the tests. The thickness ( $t_0$ ) of the unjointed part of the test specimens was also measured. During the test, each specimen was monitored with AE measurement. The bending test was carried out at room temperature with a universal testing machine (Zwick 250, Test Xpert, version 11) with a crosshead rate of 3 mm/min. Fracture processes were examined in real time using two AE sensors (micro30, Physical Acoustic Corp.), marked as S1 and S2, which were attached to the bending specimen using vacuum grease and mechanical fixture. The two AE sensors were put 46 mm apart, each one is 23mm distant from the specimen center. They were placed in such positions close to the joint ends. A two-channel AE detection system (MSTRAS 2001, Physical Acoustic Corp.) was used to record the AE data, and the AE measurement conditions were a pre-amp of 40dB, a threshold level of 40 dB, and a sampling rate of 4 MHz. The threshold was positioned at a comparatively high level so as to filter the noisy sounds coming from other emission sources. A band-pass filter under software control (pass range from 1 kHz to 1 MHz) was used for signal gain at specific frequencies. Three AE parameters were investigated: amplitude, energy, and frequency spectrum of AE signals. AE analysis may provide a way to identify and differentiate fracture sources [24,25]. Consistent with Yoon et al. [24], we ascertained that the distance between the sensor and the crack location was close enough to measure the AE characteristics. Considering the attenuation problems at high frequencies, we focused primarily on frequency bands below 400 kHz for verification of the fracture mechanisms. Fractographic analysis was also performed on damaged specimen surface and/or the fracture surface through observation by optical and scanning electron microscopy (SEM).

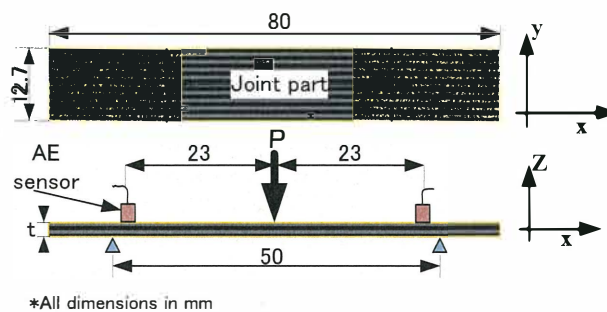


Figure 14. Illustration of an adhesive joint specimen under the three-point bending test with acoustic emission (AE) monitoring.

## 2.3. Data reduction of the adhesive joints under the bending test

The maximum load taken during the bending test of Fig.4 is used to evaluate the mechanical performance of the composite adhesive joints. It is reasonable that the joint performance should be compared with the bending strength of jointless original composite laminates. In this respect, the 'nominal' bending strength  $\sigma_1$  for every joint type can be calculated using

$$\sigma_1 = 3PL/2Wt_0^2, \quad (1)$$

where P is the maximum load value obtained from the load-deflection curve of the respective joint types, L the span length, W the specimen width, and  $t_0$  the thickness of the unjointed ligament part. The nominal bending strength assumes that the adhesive joint has a thickness equal to the unjointed ligament part. However, the thicknesses of the composite adhesive joints are varied according to the adhesive joint types, and can bring about a large variety of actual bending strength. Thus a joint efficiency ( $\eta$ ) for the various joint types is evaluated with reference to the bending strength ( $\sigma_0$ ) of the jointless original composite laminate and can be determined by a simple equation

$$\eta = \sigma_1/\sigma_0 \quad (2)$$

For S-BLJ, the nominal bending stress ( $\sigma_2$ ) on the surface at the thinned section of a joint specimen is given by

$$\sigma_2 = 3Pb/Wt_c^2, \quad (3)$$

where b is the distance between the support roller and the thinned section, and  $t_c$  the thickness of the thinned part.

## 3. Results and discussion

### 3.1. Thickness profile behaviors of the joint specimens

Table 2 shows thickness measurement data obtained for the normal BLJ. The average thicknesses were 1.83 and 3.04 mm for 6 and 10 layers, respectively. The minimum thickness and the maximum deviation were also measured for evaluating the product quality. The thickness deviation ranged to 2.8% for 6 layers and to 3.5% for 10 layers. For the S-BLJ, the average thicknesses for 5 and 7 layers were 1.46 and 2.02 mm, respectively as shown in Table 3. The thickness deviation was as high as 23%. The low minimum thickness and the large deviation indicate a bad quality that may lead to a weaker strength for the thinned part of the S-BLJ specimens. Several previous papers mentioned that the thickness variation was one of the geometrical parameters that exerted a bad influence on the performance of the adhesively bonded joints [41]. For example, a local thinning due to the thickness variation could affect the stress concentration, the strain inhomogeneity as well as the crack initiation. Ribeiro et al. [42] calculated the stress distributions along single lap adhesive joint to show a rapid increase in stress gradients around the overlap edges. Jensen et al. [43] showed a strain inhomogeneity reaching nearly 20% of the mean strain value in composite laminates under a transverse load.

Figure 5 compares the specimen thickness profiles along the specimen lengthwise direction for the three kind of joints (normal BLJ, stitched BLJ and MCLJ) with the same 6 fabric layers, and also for an 'ideal' 6-layer jointless CFRP. The stitched joints showed higher thickness deviation especially at the stitched sites. The thickness deviation was about  $\pm 0.45$  mm. Much greater thickness increase at the joint part was observed for the MCLJ. The thickness at the joint part along the joint length of 40 mm was measured to be 3.3 mm on average, which was almost twice the thickness of the jointless CFRP. This was because the number of carbon fiber covers made additional thickness exceeding the initial thickness of the adherend constructed of the original number of carbon fiber layers. This big variation in the thickness appeared along the upper surface profile of the joint part because all carbon fiber layers including the additional covers were placed on a rigid flat surface of the mold as illustrated in Figure 1c.

Table 2. Thickness profile data for normal BLJ

	Thickness, mm	minimum thickness, mm	thickness deviation, % max
6 layers	1.83(0.04)	1.78	2.8
10 layers	3.04(0.07)	2.93	3.5

Table 3. Thickness profile data for S-BLJ

	Thickness, mm	minimum thickness, mm	thickness deviation, % max
5 layers	1.46(0.08)	1.15	21
7 layers	2.02 (0.08)	1.55	23

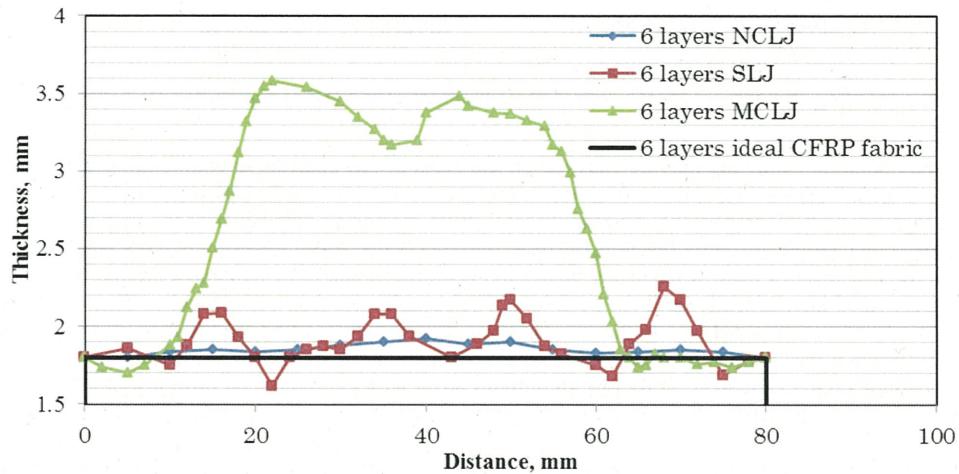


Figure 25. Typical thickness profiles for the three joints and the jointless CFRP

### 3.2. Bending strength and fracture processes of basic laminated joints

Figure 6 shows so obtained nominal bending strengths for normal and shifted BLJs. For the normal BLJ, average bending strengths for 6 and 10 carbon fiber layers were 554 and 870 MPa, respectively. It is to be noted that larger number of layers caused bigger bending strength. Tensile stress concentration at the fiber end in the surface layer under bending load might induce a similar crack initiation for both number of fiber layers. With larger number of fiber layers, however its propagation seemed to be more hindered by many neighboring reinforcing fibers. On the other hand lower bending strengths were recorded for the S-BLJ in comparison to the normal BLJ. In the VARTM process the S-BLJ had a finite gap filled with resin between the fiber ends, and the gap region in the joint was shrunk into a concave shape during curing. The thickness at the concave cross-section was measured to be smaller by 21% largely than the normal BLJ. Such large concaveness must have caused a severe notch effect, i.e. weakened bending strength. S-BLJ showed much more decrease in bending strength at bigger number of layers as manifested in Fig.6, which mostly had deeper concaveness.

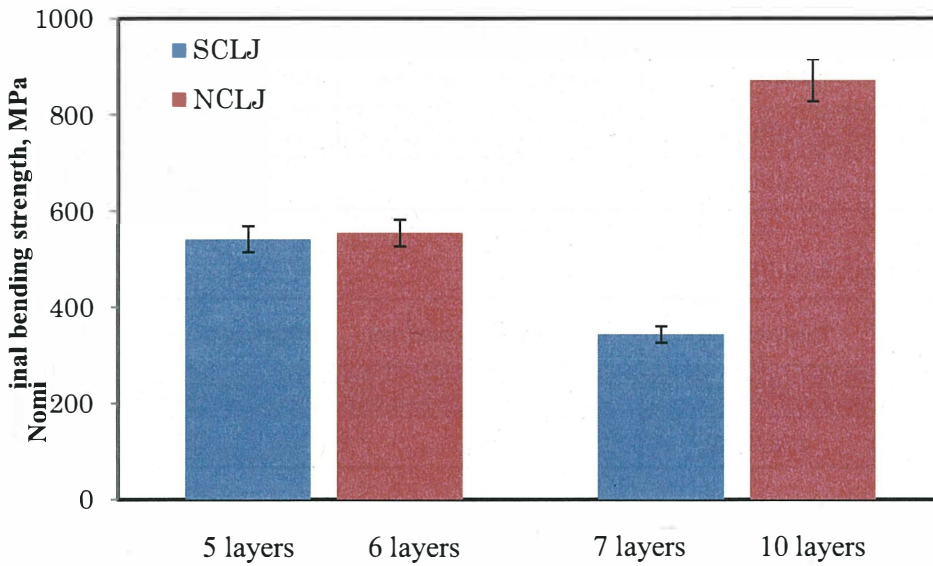


Figure 6. Bending strength results for normal basic laminated joint (BLJ) and shifted BLJ specimens

Such bending strength behaviors may be clarified on the basis of AE analysis in combination with microscopic fractography. Figure 7 shows a typical bending stress curve versus time for normal BLJ specimen of 6 layers which was recorded together with accompanying AE amplitudes. With increasing displacement the load began to increase and then dropped down largely just after reaching the peak, and finally decreased very slowly. Low amplitude emission occurred from the low level of load, whereas big amplitude emission began to be generated around 65% of the peak load, and then appeared intermittently until the peak load. High amplitudes may correspond to fiber breakages while low amplitudes may arise from crackings in the resin and/or interface between fiber and matrix, as ascertained in ref. [24,25]. In this sense it was confirmed that for normal BLJ some amount of reinforcing fibers were broken before reaching the bending strength. However only low amplitudes arose with the rapid load drop just after the peak. After finishing the large load drop, very high amplitudes were generated again, following a mild AE behavior.

Typical bending stress behavior for 5 layers S-BLJ specimens with accompanying AE amplitudes is shown in Fig.8. Clear differences from the normal BLJ appeared in this figure. The peak load level for S-BLJ was a bit lower, and the load drop proceeded in several steps and times. Big amplitude emissions began to occur at quite high level of 90% peak load prior to the peak, and sustained for a considerably long time with a slow decrease of load after the peak load. This behavior shows that around the peak load the reinforcing fibers were broken in a very different process from the normal BLJ. After passing such strong emission period, the load dropped down to around 50% of the peak load.

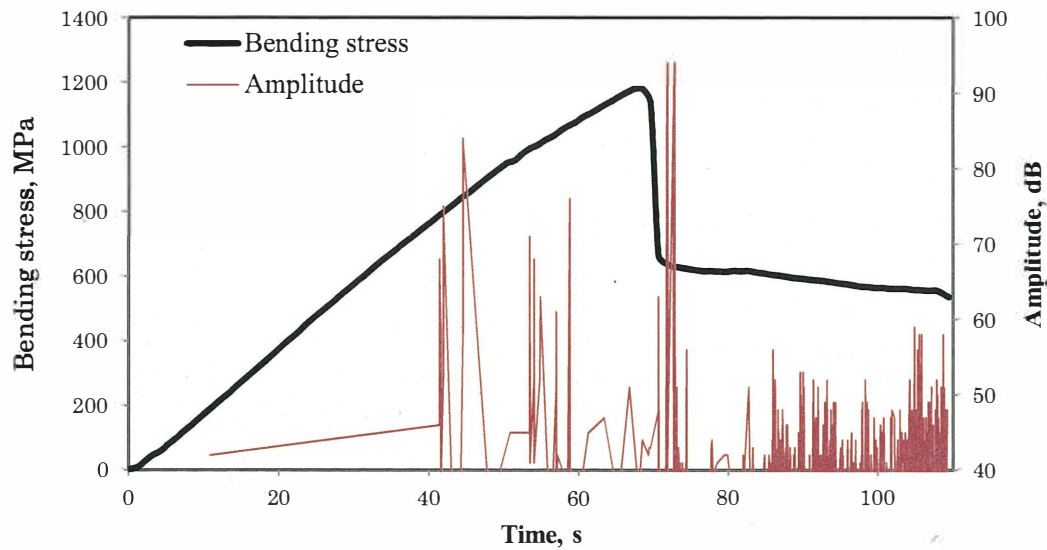


Figure 7. Typical bending stress curve versus time with accompanying AE amplitudes for normal BLJ specimen constructed of 6 fiber layers.

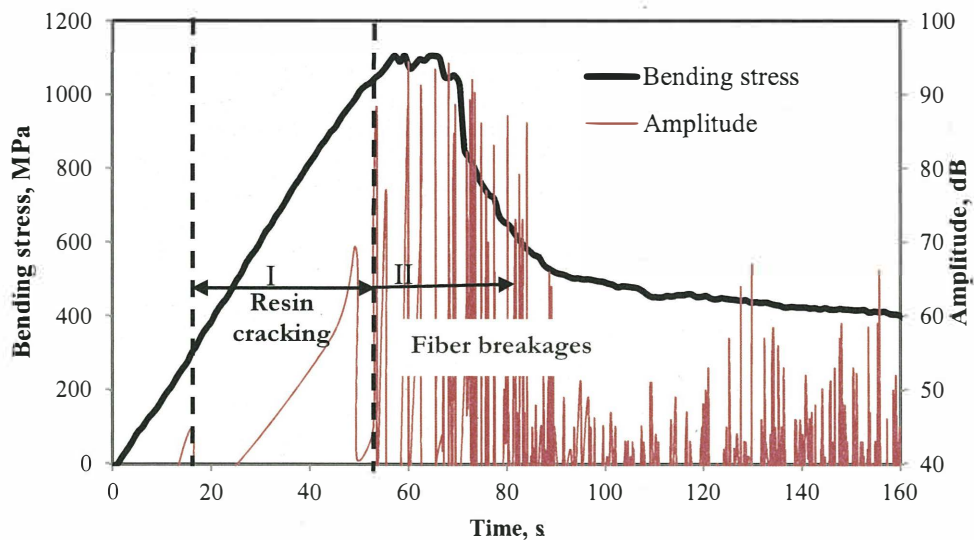


Figure 8. Typical bending stress-time curve with accompanying AE amplitude for a S-BLJ specimen of 5 fiber layers.

Fractographs taken for the normal BLJ and S-BLJ were analyzed as shown in Figure 9. For the normal BLJ specimen, a tensile bending fracture occurred along the center line of the specimen 20mm distant from the joint ends, and it induced many fiber breakages as revealed in SEM observation (see Fig.9a). It is to be noted that the tensile bending stress at the joint end of this specimen calculated by equation (3) approached only about 80% of the peak stress at the middle of the specimen. Shorter the distance of the joint end from the specimen center, larger the tensile stress arising at the joint end should be. Thus short joints can cause a fracture at the joint end because the joint ends have a weaker strength by lack of reinforcing fibers, which may lead to a lower joint strength than the long joints used in this study. In contrast, the S-BLJ showed a different failure behavior as confirmed by optical microscopic observation

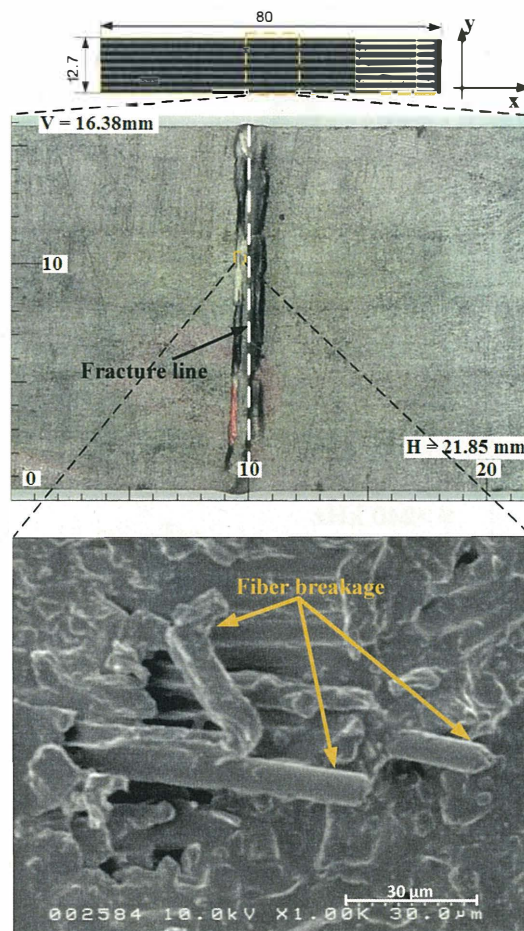
(see Fig. 9b). A resin crack initiated at the joint end where the local thinning had been formed as exhibited in Table 3, and proceeded in the loading period without observed fiber breakages along the laminate interface. This phenomenon was also confirmed in accordance with the low amplitude distribution until about 90% the peak load as shown in Fig.8. The S-BLJ can arouse a peak tensile stress at the bottom of the concaved part where the local thinned section was located. For this stress analysis, a stress concentration effect should be considered on the basis of the measured notch length  $a$  and the measured notch tip radius  $\rho_t$  by the equation:

$$\text{Stress concentration factor } (K_t) = \frac{\text{Highest stress } (\sigma_m)}{\text{Nominal stress } (\sigma_2)} = \left[ 1 + 2 * \sqrt{\frac{a}{\rho_t}} \right] \quad (4)$$

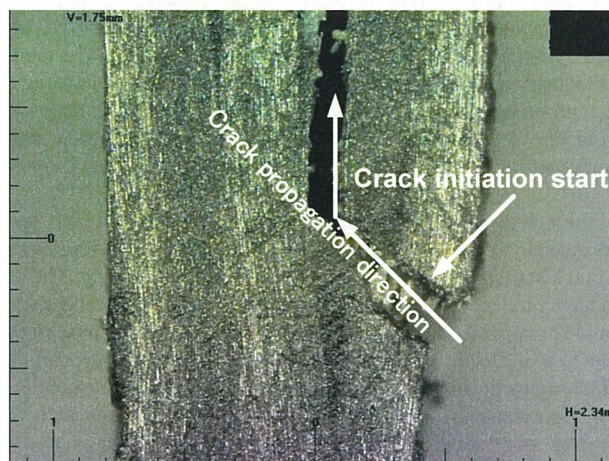
The values of  $K_t$  for S-BLJ specimens of 5 and 7 layers may be estimated as 1.34 and 1.45, respectively. The high stress values beyond the stress at the center of the joint specimen must have caused such crack initiation at the local thinned position leading to a low bending strength of S-BLJ specimens. However many fiber breakages seemed to occur just around the peak load in the process of macroscopic delamination in the joint part, as indicated by the strong amplitude emissions shown in Fig.8. It is thought that the collapse mechanism of S-BLJ specimens was significantly associated with not only the resin cracking and delamination in the loading stage but also the fractures of reinforcing fibers in the joint.

Fracture mode detection using AE frequency analysis was performed in the entire loading stage. We classified the AE features according to the fracture mode on the basis of the previous study results in which low spectral features below 160 kHz corresponded to the resin fractures, intermediate spectral features in the range of 160-240 kHz corresponded to the matrix-fiber mixed fractures, while high spectral features above 240 kHz were associated with the fiber fractures [24,25].

Figures 10 shows percentage data of AE energy accumulated until just after the peak load point according to the above mentioned frequency bands for all specimens. Different fracture behaviors were identified for the normal BLJ and S-BLJ. It was found that for the normal BLJ the AE energy spectra occurred very mostly (85 ~ 90%) in the high frequency band ( $f > 240$  kHz). Thus, the dominant fracture mode was obviously the fiber breakages. On the other hand, the S-BLJ showed that the resin crackings were in a considerable majority in the overall loading stage, because a high fraction (50 ~ 65%) of the AE energy spectrum occurred in the low frequency band ( $f < 160$  kHz). A significant portion (20~30%) of the fiber breakages was also shown in this joint, which should have arisen through the delamination process in the joint part as confirmed with the strong emissions in Fig.8.



(a)



(b)

Figure 9. Typical optical microscopy and SEM micrographs for the fracture of (a) normal BLJ with 6 layers and (b) S-BLJ with 5 layers

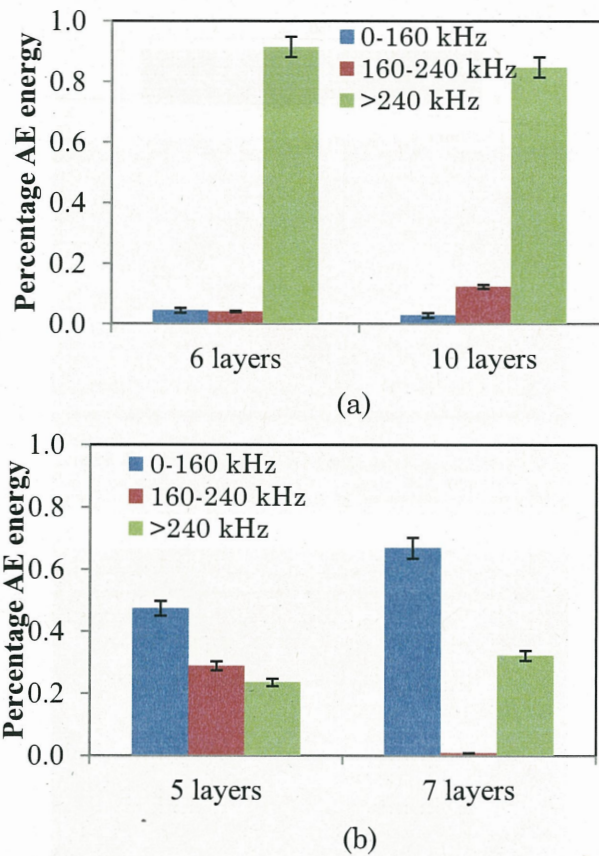


Figure 10. Percentage data of AE energy for (a) normal BLJ and (b) S-BLJ according to the three frequency bands

### 3.3. Bending strength and fracture processes of stitched laminated joints

For the stitched laminated joint (SLJ), an improved bending strength appeared as compared with the basic laminated joint. The nominal bending strength for an SLJ with 6 layers (see Figure 11) was 1405 MPa showing a high increase by 54%. A very high increase by 145% was achieved for the SLJ with 5 layers. The increase of the bending strength by the stitching depended on the number of laminated layers. The stitching showed a large effect on the joint efficiency calculated by equation (2). A high efficiency was recorded for the SLJ specimens depending on the number of layers (see Figure 11 in comparison to Fig.7). Interestingly, the SLJ with 5 layers showed a high joint efficiency exceeding 100%, which means that its endurance capacity was more than the bending strength (around 1500MPa) of the jointless CFRP laminates itself.

As seen in Figure 5, local thinned profiles thus notches formed at the stitched sites for the SLJ. With this bending test, the fracture initiated to propagate not at the joint ends but along the middle line around the center of all the SLJ specimens. The macroscopic crack started at one of the notches formed by stitching. The stitches which applied across the carbon fiber layers should have hindered the crack initiation along the interface between the fiber layers at the joint ends. Abusrea and Arakawa [11] confirmed through the tensile test that the stitching improved the tensile strength of the staircase adhesive joint due to a bidirectional fiber structure with additional perpendicular reinforcement function. Plain and Tong [26] used a stitching technique to improve mode I and II fracture toughness for laminated composites. Velmurugan et al. [27] showed some retarded crack initiation and delayed crack growth when a stitching was applied to a cylindrical shell subjected to axial compression. For bending load, Chung et al. [28] found that the stitching improved the strength of CFRP and KFRP by 25%. Adanur and Tsao [29] reported an improvement in the flexural properties of KFRP and CFRP even when stitched at a comparatively low density. The through-thickness stitching performed by many researchers improved the mechanical performances of the laminated adhesive joints. Aymerich et al. [37] reported for single-lap composite joints that the stitching prolonged the duration of the crack propagation phase under fatigue loading. Sawyer [38] confirmed also an improvement of the static failure strength up to 38% by using a stitching into the single lap bonded composite joints. Jain et al. [39] also showed that the stitched adhesive joints achieved a large increase by 36.5% in the peak load compared to the unstitched laminated joints manufactured using

the RTM technique.

With increasing the thickness and/or the layup number, the average bending strength decreased to a low value of 1144 MPa for the 7 layers SLJ. The AE energy spectra and SEM analyses were conducted for the SLJ. Figure 12 shows typical percentages of AE energy in the three frequency bands for stitched laminated joints with 5, 6, and 7 layers. The SLJ generated a higher percentage (around 74%) of AE energy in the high frequency band (>240 kHz). This behavior was quite consistent for the various layup numbers in the joints. Such behavior of high frequency emissions indicates that fiber breakages dominated the fracture process up to the peak load for the SLJ type. The effectiveness of stitching in the bending strength decreased considerably at higher thicknesses. A reason of the low strength with thick SLJ seems to be related with the results that many reinforcing fibers and stitched yarns were broken in the loading stage prior to the peak load. This can be attributed to the fact that with increasing the layup thickness the stitching formed larger notches partly filled with resin in the skin layer [11]. This fracture behavior was confirmed by a SEM photographs analysis, where many fiber breakages appeared in the fracture initiation region for the thick SLJ specimens with 7 layers.

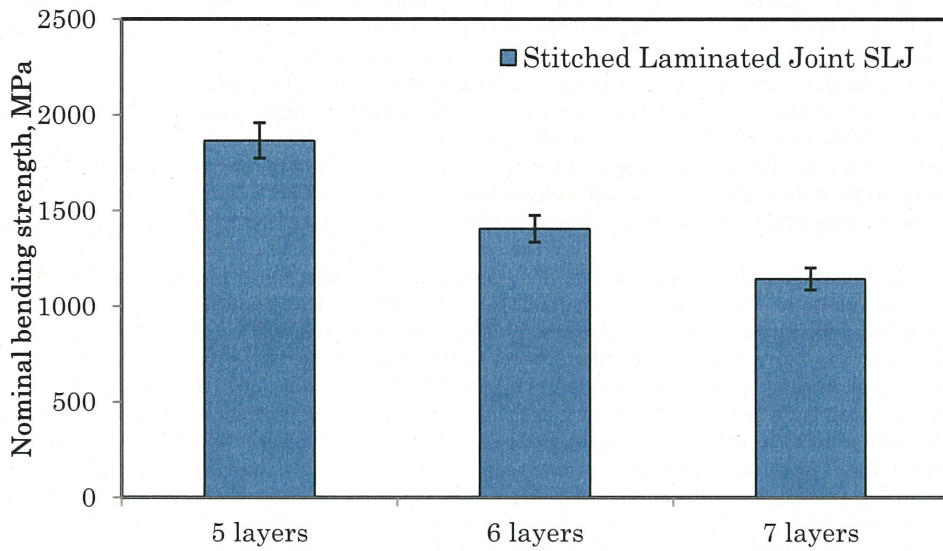


Figure 11. Nominal bending strengths for SLJ with various layup numbers in the joint

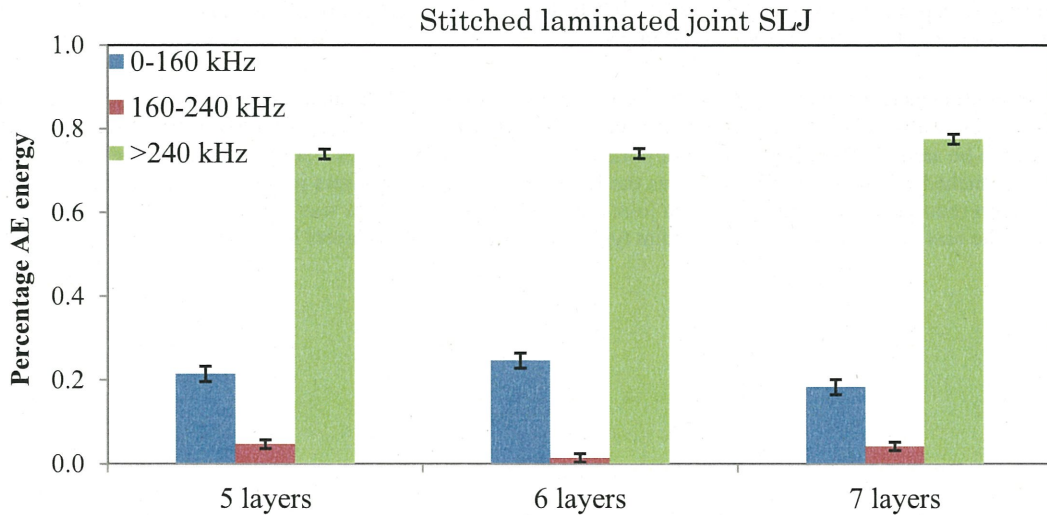


Figure 12. Percentage data of AE energy for SLJ according to the three frequency bands

### 3.4. Bending strength and fracture processes of multiple-covers laminated joints

MCLJ achieved much higher nominal bending strength than the basic laminated joint. As shown in Fig.13 the MCLJ with 6 layers had a bending strength of 2.33 GPa, which represented the maximum bending performance among all the tested MCLJ types. The strength value indicated a drastic increase by 321% than the normal BLJ and a considerable increase by 66% than the stitched BLJ. The other MCLJ with 10 layers showed a decreasing value of 1.29 MPa, still larger than the stitched BLJ. The increase in the bending strength for the MCLJ can be explained by simple stress analysis: The insertion of seven extra carbon fiber covers as illustrated in Fig.2c made a thick laminated joint which could work as a multiple-bonded double lap joint (DLJ). Because the MCLJ specimen was manufactured with the VARTM method, the joint part smoothly changed to the thin ligament adherend by filling the resin to the corner between the thick joint part and the thin adherend. The thickness of the joint part was almost twice as large as that of the adherend. In this case the tensile stress at the bottom surface of the joint part is calculated to be one-fourth of that for the corresponding BLJ according to equation (1) under the same bending load. The macroscopic fracture shown in Fig.14 proceeded at the center line of the joint part, which was similarly observed also for the normal BLJ specimen (Fig.9). When the same material strength is assumed for both the BLJ and MCLJ, bending strength of MCLJ should be four times as large as that for BLJ, which agreed well with the above bending strength result about 4.21 times larger than the BLJ. The small mismatch of the bending strength data between measurement and calculation might be considered due to the fluctuated deviation in the thickness of the joint part (see Fig.5).

On the other hand, the thickness change from the adherend to the joint part was measured as shown in Fig.5, which should induce a peak stress concentrated at the local site just where the joint began from the adherend. However all the fracture events only occurred in the middle of the joint part, which indicates that the peak stress at the boundary site of the joint part did not reach the tensile strength of the MCLJ specimens. The peak stress site and the fracture initiation might occur probably at the end of the joint part with decreasing the length of MCLJ part in comparison to the test span. In this case the bending strength mechanisms should be different on account of the fracture process arising at the joint ends.

The macroscopic fracture along the center line of the joint part was similar for all the MCLJ specimens with various layers adopted in this study. The MCLJs with 5, 7 and 10 layers showed lower bending strengths than the MCLJ with 6 layers. The low bending strength for the 5 layers joint might be predicted with the simple stress theory of equation (1) stated above for the 6 layers joint, in that the 5 layers joint had an average thickness larger by about 10% than that expected from the normal layup thickness. The rather thicker 5 layers joint was due to the more resin infiltration in the VARTM process than the 6 layers joint. However the decreasing bending strength of MCLJs with 7 and 10 layers could not be clarified with the simple stress theory, but be attributed to a large defect formation in the thick layup joints. For the 7 and 10 layers joint, extra fiber covers were inserted between the layers causing much thicker joint part which could contain bigger voids during the VARTM process. The existence of critical large voids might induce an easy fracture of the thick MCLJ. Figure 15 shows typical percentages of AE energy in the three frequency bands for MCLJs with 5, 6, 7 and 10 layers. Most MCLJ specimens emitted a high percentage (60~ 98%) of AE energy in the high frequency band (>240 kHz). This represents that fiber breakages were very dominant in the fracture process until the peak load as confirmed again in the SEM observation of Fig.14. The bending strength behaviors of Fig.13 which largely depended on the thicknesses of MCLJs are considered to have been associated mainly with a fracture procedure of the carbon fabric during the loading stage.

Joint efficiencies for all the types of laminated adhesive joints were calculated using equation (2) in comparison to the jointless CFRP laminates as summarized in Fig.16. The average bending strength of the jointless CFRP was measured to be around 1500 MPa[C1]. For normal BLJ, joints efficiencies were distributed in the range of 24% ~ 58%. For stitched LJ, the joint efficiency was the largest (124%) at the 5 layers joint, however the increasing layers over 5 layers reduced significantly. Excellent joint efficiency exceeding 100% was also shown for the MCLJs with 5 ~ 7 layers. The best efficiency among all the joint types was obtained at the 6 layers MCLJ.

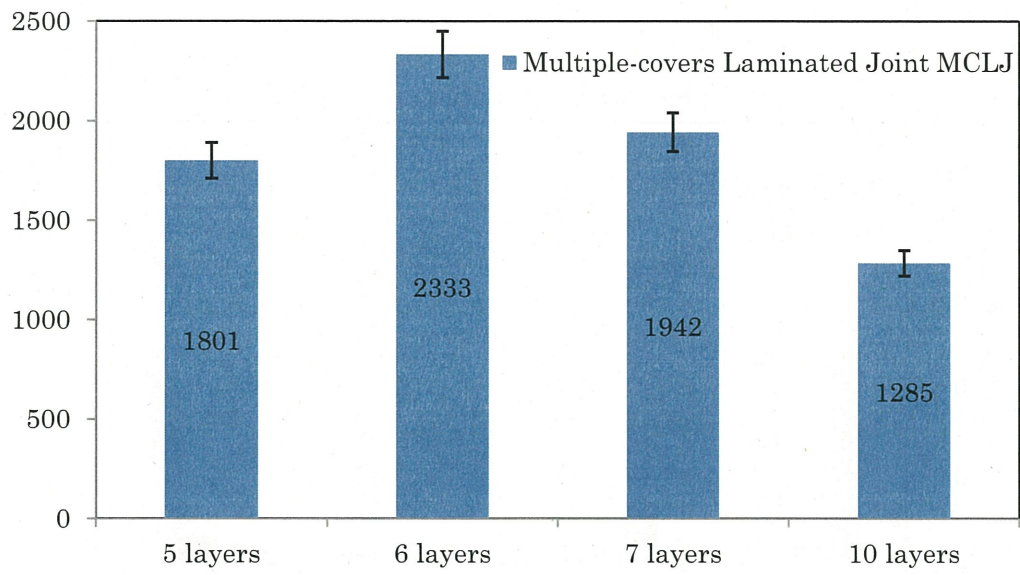


Figure 13. Nominal bending strengths for MCLJ with various layers in the joint

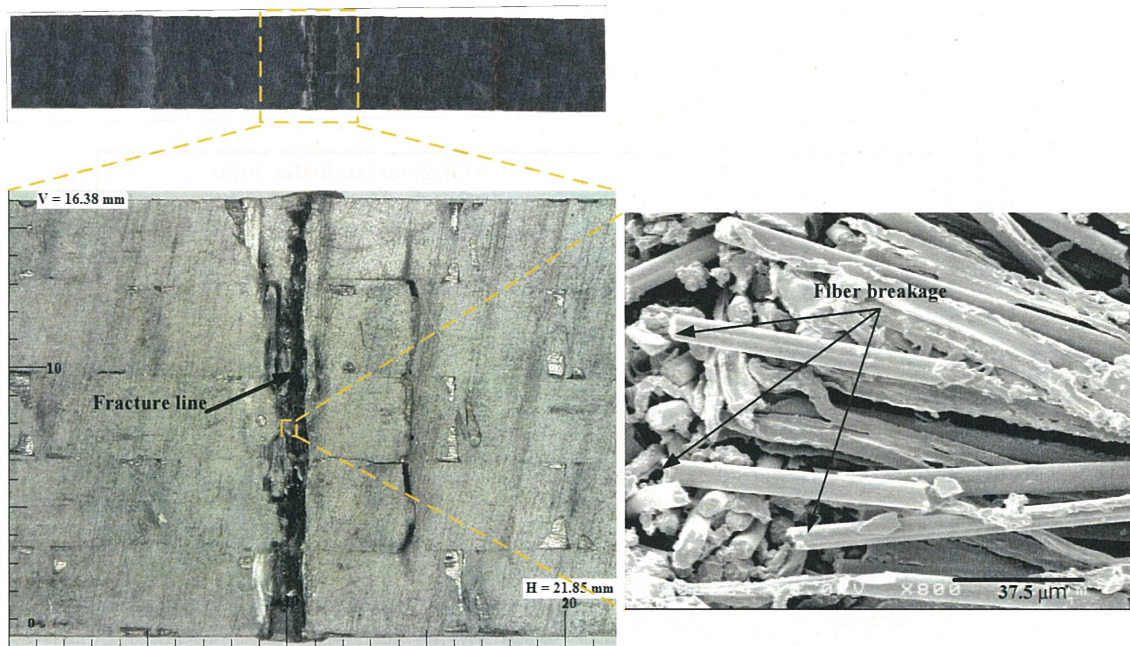


Figure 14. Typical optical and SEM photographs for the fracture of MCLJ with 6 layers

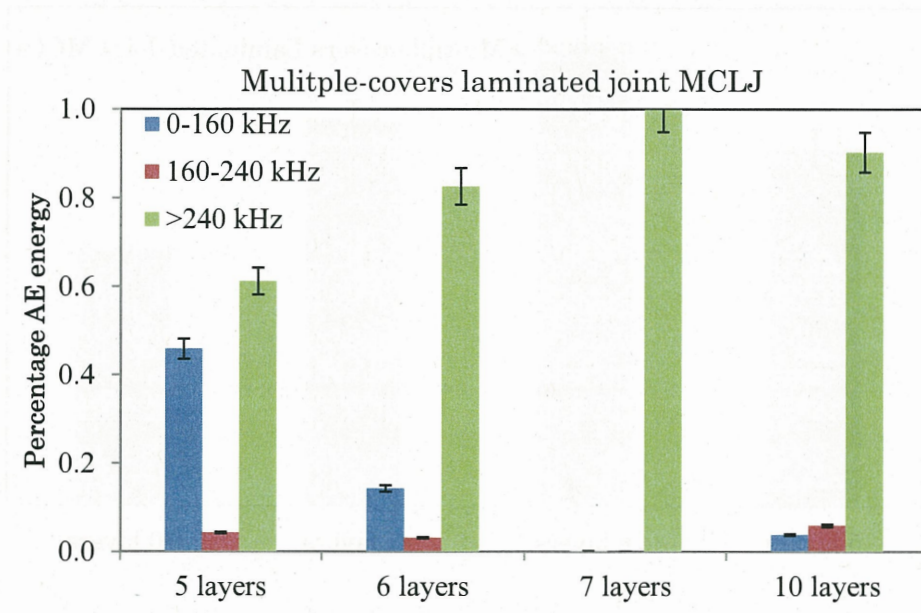


Figure 15. Percentage data of AE energy for MCLJ according to the three frequency bands

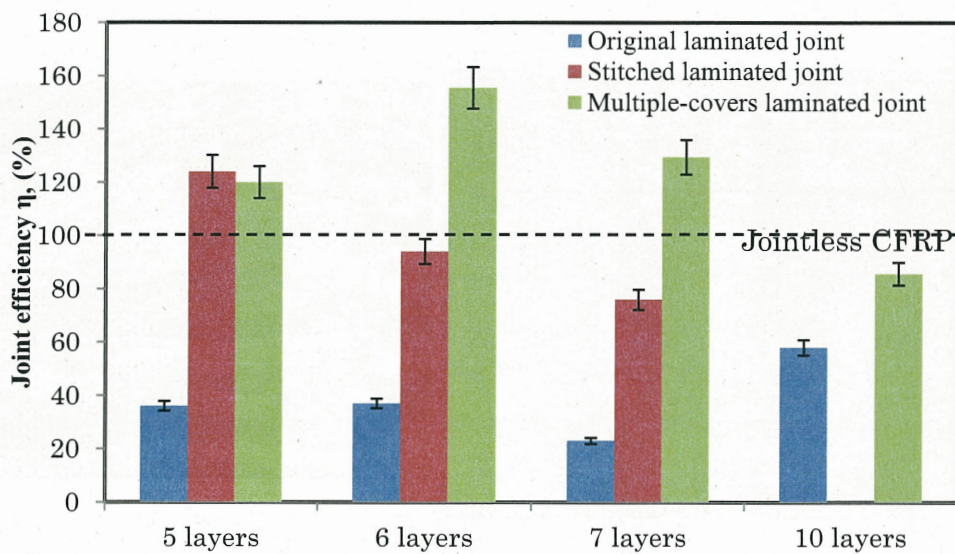


Figure 16. Joint efficiencies for the various laminate joints as compared with jointless CFRP

## 4. Conclusions

The laminated adhesive joints were made using VARTM process. Three types of laminated joints were studied: conventional basic laminated joint (BLJ), stitched laminated joint (SLJ), and multiple-covers overlapped laminated joint (MCLJ). All joint specimens were tested under the three-points bending load to evaluate their strength performances in terms of the nominal bending strength. For normal BLJ, increasing layers improved the bending strength while a shifted layup formed a concave notch where larger number of layers caused weaker bending strength. Acoustic emission analysis and fractographic observation confirmed that the fracture mode for the normal BLJ was mainly fiber breakages prior to the maximum load point which dominated the bending strength mechanisms of normal BLJ. The shifted layup in the joint caused the fracture initiation mode to be the resin cracking at the notch site. On the other hand, stitched laminated joints (SLJs) showed much improved bending strength compared to the BLJ. The SLJ with 5 layers showed excellent joint efficiency around 124%. The MCLJ achieved superior bending strength in which the joint efficiency for 5 ~ 7 layers joints exceeded 120%. The best efficiency among all the joint types was obtained at the 6 layers MCLJ. It was confirmed by combined AE and microscopic analysis that fiber breakages were very dominant, i.e. fiber reinforcement caused the superior bending strength for the two joint types of SLJ and MCLJ. Consequently, stitching and multiple covers insertion reinforced clearly the adhesive joints, in which some optimal layup thickness and surface profile perfectness formed by the VARTM were required to show the best bending strength.

## ACKNOWLEDGMENT

This work was partly supported by a research grant from the Japan Society for Promotion of Science (#JP26630496), and by the Collaborative Research Program of Research Institute for Applied Mechanics, Kyushu University.

## References

- [1]. T. Keller, T. Vallée. Adhesively bonded lap joints from pultruded GFRP profiles. Part I: stress-strain analysis and failure modes. *Composites: Part B* 36 (2005), pp. 331–340
- [2]. L. Burns, A.P. Mouritz, D. Pook, S. Feih. Strengthening of composite T-joints using novel ply design approaches. *Composites: Part B* 88 (2016), pp. 73–84.
- [3]. Shufeng L, Xiaoquan C, Qian Z, Jie Z, Jianwen B, and Xin G. An investigation of hygrothermal effects on adhesive materials and double lap shear joints of CFRP composite laminates. *Composites: Part B* 91 (2016), pp. 431–440
- [4]. Akderya, T., Kemiklioğlu, U., & Sayman, O. (2016). Effects of thermal ageing and impact loading on tensile properties of adhesively bonded fibre/epoxy composite joints. *Composites Part B: Engineering*, 95, 117–122. <https://doi.org/10.1016/j.compositesb.2016.03.073>
- [5]. Abusrea, M. R., & Arakawa, K. (2016). Improvement of an adhesive joint constructed from carbon fiber-reinforced plastic and dry carbon fiber laminates. *Composites Part B: Engineering*, 97, 368–373. doi:10.1016/j.compositesb.2016.05.005
- [6]. Xiang, J., Zhao, S., Li, D., & Wu, Y. (2017). An improved spring method for calculating the load distribution in multi-bolt composite joints. *Composites Part B: Engineering*, 117, 1–8. <https://doi.org/10.1016/j.compositesb.2017.02.024>
- [7]. Friedrich, C., & Hubbertz, H. (2014). Friction behavior and preload relaxation of fastening systems with composite structures. *Composite Structures*, 110, 335–341. doi:10.1016/j.compstruct.2013.11.024
- [8]. Lee, Y.-H., Lim, D.-W., Choi, J.-H., Kweon, J.-H., & Yoon, M.-K. (2010). Failure load evaluation and prediction of hybrid composite double lap joints. *Composite Structures*, 92(12), 2916–2926. doi:10.1016/j.compstruct.2010.05.002
- [9]. Oplinger JW. Mechanical fastening and adhesive bonding. In: Peters ST, editor. *Handbook of composites*. New York: Springer; 1998.
- [10]. Abusrea, M., R., Jiang, S., Chen, D., Arakawa, K., . Novel CFRP Adhesive Joints and Structures for Offshore Application. *International Journal of Chemical, Molecular, Nuclear, Materials and Metallurgical Engineering* 9 (9), 2015
- [11]. Abusrea, M., R., and Arakawa, K., Evaluation of the strength of CFRP adhesive joints manufactured using VARTM. *Advanced Experimental Mechanics, Vol.1* (2016) 111-114.

- [12]. **Chen**, D., Arakawa, K., Jiang, S., . Novel joints developed from partially un-moulded carbon-fibre-reinforced laminates. *Journal of Composite Materials*, 2015, Vol. 49(14) 1777–1786.
- [13]. Ascione, F. (2016). The influence of adhesion defects on the collapse of FRP adhesive joints. *Composites Part B: Engineering*, 87, 291–298. doi:10.1016/j.compositesb.2015.10.033
- [14]. Heim, D., Hartmann, M., Neumayer, J., Klotz, C., Ahmet-Tsaous, Ö., Zaremba, S., & Drechsler, K. (2013). Novel method for determination of critical fiber length in short fiber carbon/carbon composites by double lap joint. *Composites Part B: Engineering*, 54, 365–370. doi:10.1016/j.compositesb.2013.05.026
- [15] Salih Akpinar. The strength of the adhesively bonded step-lap joints for different step numbers. *Composites: Part B* 67 (2014) 170–178 doi:10.1016/j.compositesb.2014.06.023
- [16] Löbel, T., Kolesnikov, B., Scheffler, S., Stahl, a., & Hühne, C. (2013). Enhanced tensile strength of composite joints by using staple-like pins: Working principles and experimental validation. *Composite Structures*, 106, 453–460. doi:10.1016/j.compstruct.2013.06.020
- [17] Mouritz AP, Chang P, Cox BN. Fatigue properties of z-pinned aircraft composite materials. *ICAS Int Cong Aeronaut Sci* 2006.
- [18] Dransfield, K. A., Jain, L. K., & Mai, Y.-W. (1998). On the effects of stitching in CFRPs—I. mode I delamination toughness. *Composites Science and Technology*, 58(6), 815–827. doi:10.1016/S0266-3538(97)00229-7
- [19] Heß, H., & Himmel, N. (2011). Structurally stitched NCF CFRP laminates. Part 1: Experimental characterization of in-plane and out-of-plane properties. *Composites Science and Technology*, 71(5), 549–568. doi:10.1016/j.compscitech.2010.11.012
- [20] Kim, J. H., Park, B. J., & Han, Y. W. (2004). Evaluation of fatigue characteristics for adhesively-bonded composite stepped lap joint. *Composite Structures*, 66(1), 69–75. doi:10.1016/j.compstruct.2004.04.023
- [21] Abe K-i, Ohya Y. An investigation of flow fields around flanged diffusers using CFD. *Journal of Wind Engineering and Industrial Aerodynamics*. 2004;92(3–4):315-330.
- [22] Abe K, Nishida M, Sakurai A, Ohya Y, Kihara H, Wada E, et al. Experimental and numerical investigations of flow fields behind a small wind turbine with a flanged diffuser. *Journal of Wind Engineering and Industrial Aerodynamics*. 2005;93(12):951-970.
- [23] Ohya Y, Karasudani T. A Shrouded Wind Turbine Generating High Output Power with Wind-lens Technology. *Energies*. 2010;3(4):634-649.
- [24]. Yoon, SY., Arakawa K., Han, SW., Chen, D., and Choi, NS.,. Effect of Compaction Treatment on Laminated CFRP Composites Fabricated by Vacuum-Assisted Resin-Transfer Molding. 2015; DOI:10.1002/pc.23578
- [25]. Gu, J.-U., Yoon, H.-S., & Choi, N.-S. (2012). Acoustic emission characterization of a notched aluminum plate repaired with a fiber composite patch. *Composites Part A: Applied Science and Manufacturing*, 43(12), 2211–2220. doi:10.1016/j.compositesa.2012.07.018
- [26]. Plain, K. P., & Tong, L. (2011). An experimental study on mode I and II fracture toughness of laminates stitched with a one-sided stitching technique. *Composites Part A: Applied Science and Manufacturing*, 42(2), 203–210. doi:10.1016/j.compositesa.2010.11.006
- [27]. Velmurugan, R., Gupta, N. K., Solaimurugan, S., & Elayaperumal, A. (2004). The effect of stitching on FRP cylindrical shells under axial compression. *International Journal of Impact Engineering*, 30(8), 923–938. doi:10.1016/j.ijimpeng.2004.04.007
- [28]. Chung, W. C., Jang, B. Z., Chang, T. C., Hwang, L. R., & Wilcox, R. C. (1989). Fracture behavior in stitched multidirectional composites. *Materials Science and Engineering: A*, 112, 157–173. doi:10.1016/0921-5093(89)90355-9
- [29]. S. Adanur, Y.P. Tsao. Stitch bonded textile structural composites Proc. 26th Int. SAMPE Tech. Conf. (1994), pp. 25–34

- [30]. Mitsubishi Rayon CO., LTD., Profile Department, [www.mrc.co.jp](http://www.mrc.co.jp)
- [31]. Zhao, T., Palardy, G., Villegas, I. F., Rans, C., Martinez, M., & Benedictus, R. (2017). Mechanical behaviour of thermoplastic composites spot-welded and mechanically fastened joints: A preliminary comparison. *Composites Part B: Engineering*, 112, 224–234. <http://doi.org/10.1016/j.compositesb.2016.12.028>
- [32]. Ghasemnejad, H., Argentiero, Y., Tez, T. A., & Barrington, P. E. (2013). Impact damage response of natural stitched single lap-joint in composite structures. *Materials & Design*, 51, 552–560. <http://doi.org/10.1016/j.matdes.2013.04.059>
- [33]. Cheuk, P. T., & Tong, L. (2002). Failure of adhesive bonded composite lap shear joints with embedded precrack. *Composites Science and Technology*, 62(7–8), 1079–1095. [http://doi.org/10.1016/S0266-3538\(02\)00054-4](http://doi.org/10.1016/S0266-3538(02)00054-4)
- [34]. Tan, K., Watanabe, N., & Iwahori, Y. (2011). Stitch fiber comparison for improvement of interlaminar fracture toughness in stitched composites. *Journal of Reinforced Plastics and Composites*, 30(2), 99–109. <http://doi.org/10.1177/0731684410383065>
- [35]. Callister, William D., and David G. Rethwisch. *Materials Science and Engineering: An Introduction*. 7th ed. Hoboken, NJ: Wiley, 2007. Print.
- [36]. Behnia, A., Ranjbar, N., Chai, H. K., Abdullah, A. I., & Masaeli, M. (2017). Fracture characterization of multi-layer wire mesh rubberized ferrocement composite slabs by means of acoustic emission. *Journal of Cleaner Production*, 157, 134–147. <http://doi.org/10.1016/j.jclepro.2017.03.192>
- [37]. Aymerich, F., Onnis, R., & Priolo, P. (2005). Analysis of the fracture behaviour of a stitched single-lap joint. *Composites Part A: Applied Science and Manufacturing*, 36(5), 603–614. <http://doi.org/10.1016/j.compositesa.2004.08.003>
- [38]. J. W. Sawyer. "Effect of stitching on the strength of bonded composite single lap joints", *AIAA Journal*, 23 (11), 1985, pp. 1744-1748
- [39]. Lalit K. Jain, K. H. Leong, Yiu-Wing Mai and Liyong Tong. "Effect of Through-Thickness Stitching on the Fatigue Life of Composite Single-Lap Joints", *Applied Composite Materials*, 5 (6), 1998, pp 399-409
- [40]. Gray, P. J., O'Higgins, R. M., & McCarthy, C. T. (2014). Effect of thickness and laminate taper on the stiffness, strength and secondary bending of single-lap, single-bolt countersunk composite joints. *Composite Structures*, 107, 315–324. <http://doi.org/10.1016/j.compstruct.2013.07.014>
- [41]. Budhe, S., Banea, M. D., de Barros, S., & da Silva, L. F. M. (2017). An updated review of adhesively bonded joints in composite materials. *International Journal of Adhesion and Adhesives*, 72, 30–42. <http://doi.org/10.1016/j.ijadhadh.2016.10.010>
- [42]. Jensen, E. M., Leonhardt, D. A., & Fertig, R. S. (2015). Effects of thickness and fiber volume fraction variations on strain field inhomogeneity. *Composites Part A: Applied Science and Manufacturing*, 69, 178–185. <http://doi.org/10.1016/j.compositesa.2014.11.019>
- [43]. Jensen, E. M., Leonhardt, D. A., & Fertig, R. S. (2015). Effects of thickness and fiber volume fraction variations on strain field inhomogeneity. *Composites Part A: Applied Science and Manufacturing*, 69, 178–185. <http://doi.org/10.1016/j.compositesa.2014.11.019>
- [44]. Aymerich F. Effect of stitching on the static and fatigue performance of co-cured composite single-lap joints. *J Compos Mater*, 38, 2004; pp. 243–257

## 国際化推進共同研究概要

No.15

タイトル: Modeling the crystal growth of nitrides thin films from the process to the defects generation : case of AlN by chemical vapor deposition

研究代表者: Mercier, Frederic

所内世話人: 柿本 浩一

概要: 真空紫外光の光源に必須な AlN の結晶成長に関する共同研究を行った。応用力学研究所で従来開発されてきたシリコンや GaN の計算コードを用いて AlN の結晶成長を記述できるコード開発を共同で行った。その結果、AlN の結晶成長の解析が可能となった。さらに、このコードを CVD に拡張するべく、今後とも共同研究を継続していく。

# Collaboration report

Frederic Mercier  
SIMAP, France

My research is focused on the thin film fabrication with a special emphasis on the development of chemical vapor deposition-based techniques of nitrides. My work is aimed at understanding the fundamental mechanisms that control the materials deposition processes and the final properties. Development of oriented and epitaxial thin films serve as a basis for fundamental understanding and for improved functional properties.

Within this context, this research project is focused on Aluminium nitride (AlN), which is of technological importance for energy applications (UV-LED, laser diodes and high power and temperature electronic device, energy harvesters). Despite its strong potential, the scientific and technological difficulties hinder the development of this material. For example, the performance of white and UV-based AlN diodes is limited by the density of crystalline defects in the active layers of the devices. Such the defects are generated during the material fabrication in a poorly controlled process.

The aim of the report is to understand the link between the process conditions and the occurrence of defects (nucleation and multiplication) during the chemical vapor deposition of AlN. Toward this objective, a first step has been reached by The Crystal Growth Dynamics Section lab, who developed very recently a model that describes defects generation in crystalline materials. Originally developed on silicon, then on GaN at RIAM, I successfully extended it to AlN in order to understand the evolution of the plastic deformation during its crystal growth.

The aim of the proposal is to understand the link between the process conditions and the occurrence of defects (nucleation and multiplication) during the chemical vapor deposition of AlN. Toward this objective, one step has been reached by the SIMAP lab who developed a multiscale model of AlN deposition by CVD which allows the quantification of local values like supersaturation. Another step has been reached by the Crystal Growth Dynamics Section lab who developed very recently a model that describes defects generation in crystalline materials, originally developed on silicon, then on GaN. The aim of this project is to unify this two modeling approaches in order to understand the evolution of the plastic deformation of AlN crystalline thin films

in the CVD process. We could discuss the details of growth mechanism by the collaboration.

真空紫外光の高原に必須な AlN の結晶成長に関する共同研究を行った。応用力学研究所で従来開発されてきたシリコンや GaN の計算コードを用いて AlN の結晶成長を記述できるコード開発を共同で行った。その結果、AlN の結晶成長の解析が可能となった。さらに、このコードを CVD に拡張するべく、今後とも共同研究を継続していく。

## 国際化推進共同研究概要

No.16

タイトル: Computational and experimental analysis for marine renewable energy development.

研究代表者: WAN, Decheng

所内世話人: 胡 長洪

概要: 今年度の国際化推進共同研究「Computational and experimental analysis for marine renewable energy development」に関して、共同研究・研究集会とも予定通り実施した。共同研究成果について、2編の国際学会論文を投稿し採択された。研究集会について、世話人が担当した特定研究の研究集会と共同開催で、外国から9名、日本から約30名の参加者があり、海洋再生可能エネルギー開発に関する有意義な国際研究集会となった。

## **Computational and experimental analysis for marine renewable energy development**

### **Purpose**

Marine renewable energy devices are usually installed in a sea area where severe environmental conditions have to be considered. On the other hand, cost control is strictly required for those devices in order to pass economic evaluations. Therefore for successful design of those devices, accurate numerical methods as well as efficient experimental methods are required to evaluate the hydro- and aerodynamic performance of these devices. This joint research project aims to provide an opportunity for researchers, especially younger researchers in SJTU and RIAM, to exchange their knowhow on development of computational and experimental tools for the purpose.

### **Research Plan**

- (1) Carry out collaborative research between SJTU and RIAM, in the area of advanced modeling of unsteady hydrodynamic and aerodynamic forces interacting on offshore floating wind turbine, to provide a benchmark for validation and comparison of various analytical, simulation and experimental models on the study of the floating offshore wind turbine problem.
- (2) Evaluate the system's responses of 6DOF motions, which are excited by both wave and wind under various conditions as well as the rotation of blades.
- (3) Organize an international symposium in the end of each fiscal year, in which relative researchers will present and discuss their research results

The members involved in this collaborative research are shown in the following table.

Researcher's Name	Name of University or Institute	Present Status or Grade (graduate students)	Researcher role
Decheng Wan	SJTU	Professor	Representative person (CFD)
Min Zhao	SJTU	Associate Professor	Co-researcher (Experiment)
Lu Zou	SJTU	Lecturer	Co-researcher (CFD)
Yang Huang	SJTU	PhD student	Co-researcher (CFD)
Makoto Sueyoshi	RIAM	Assistant professor	Co-researcher (experiment)
Cheng Liu	RIAM	Posdoc	Co-researcher (CFD)
Changhong Hu	RIAM	Professor	RIAM Attendant

## Summary of Collaboration Research

In 2017, one of the most critical factors in wind farm, the inter-turbine spacing has been studied by CFD simulations. This parameter has a great influence on aerodynamic power output, wind speed deficit, lifetime, and wake vortex structure. Considering the uniform inflow conditions, the effects of inter-turbine spacing changing from three to nine times of rotor diameter on aerodynamics for wind farms containing two NREL 5MW baseline wind turbines in tandem layout are analyzed using actuator line model and CFD method. The RANS equation with  $k-\omega$  SST turbulence model was solved in the simulations conducted in the OpenFOAM. From the study, it is concluded that the inter-turbine spacing has significant effects on the aerodynamic power and wake characteristics. The aerodynamic power output of the downstream wind turbine exits sharp fluctuation before power output of the downstream wind turbine is becoming steady. Furthermore, periodic oscillation whose period is about the one-third of rotor rotating period can be also concluded from the study. Moreover, there is strong wake interaction which will impact the aerodynamics for wind farms seriously.

Two international conference papers related to this joint research project in 2017 are listed as follows.

- 1) Yong Ai, Decheng Wan, Changhong Hu, Effects of Inter-Turbines Spacing on Aerodynamics for Wind Farms Based on Actuator Line Model, Proceedings of the Twenty-seven (2017) International Ocean and Polar Engineering Conference San Francisco, California, USA, June 25-30, 2017 , pp. 386-394
- 2) Yang Huang, Decheng Wan, Changhong Hu, Coupled Aero-hydrodynamic Analysis on a Floating Offshore Wind Turbine under Extreme Sea Conditions, Proceedings of the Twenty-seven (2017) International Ocean and Polar Engineering Conference San Francisco, California, USA, June 25-30, 2017 , pp. 395-402

As a main event of this international joint research project, 'International RIAM Symposium on Ocean Renewable Energy Technologies and Related Computational and Experimental Researches' was held on January 22-23, 2018. On the symposium, overseas scholars are invited to present their recent researches on ocean renewable energy development.

The research budget provided for this international joint research has been used to support part of the travel expenses of the following 5 scholars to attend the symposium.

1. Decheng Wan, Professor, Shanghai Jiao Tong University, China
2. Shiu-Wu Chau, Professor, National Taiwan University, Taiwan, R.O.C.
3. Di Deng, PhD Student, Shanghai Jiao Tong University, China
4. Yang Huang, PhD Student, Shanghai Jiao Tong University, China
5. Xiao Wen, PhD Student, Shanghai Jiao Tong University, China

The program of the symposium is as follows.

# PROGRAM

Date: January 22-23, 2018

Place: Meeting Room at 2nd Floor, RIAM, Kyushu University

## 22 January (Monday)

13:00 - 13:10	<i>Opening Address</i>	<b>Changhong Hu</b>
---------------	------------------------	---------------------

### *Session 1*

13:10 - 14:00	<b>Yonghwan Kim</b> (Seoul National University, Korea) <i>Invited Lecture</i> Statistical Probability Modeling of Deck Slamming on Offshore Structures
14:00 - 14:30	<b>Xiao Wen, Decheng Wan</b> (Shanghai Jiao Tong University, China) Numerical Simulations of Sloshing Flows in an Elastic Tank by MPSFEM-SJTU Solver
14:30 - 15:00	<b>Jin Huang, Bin Teng</b> (Dalian University of Technology, China) Numerical Simulation of Wave Slamming of Two-Dimensional Bodies
15:00 - 15:30	Coffee break

### *Session 2*

15:30 - 16:00	<b>Taiga Asaumi, Masashi Kashiwagi</b> (Osaka University) Cloaking of a Vertical Cylinder using Variable Bathymetry
16:00 - 16:30	<b>D. Ohno, Y. Higo, H. Iwashita</b> (Hiroshima University) Hydrodynamics and Motions of a FOWT in the Low-Speed Current
16:30 - 17:00	<b>Isshiki Hiroshi</b> (Institute of Numerical Analysis) Generation of Curvilinear Coordinates for Numerical Analysis
17:00 - 17:30	<b>Patxi Garcia Novo, Yusaku Kyojuka</b> (Nagasaki University) Estimation of Tidal Peak Velocity by an Empirical Approach
18:00 - 20:00	Dinner Party

23 January (Tuesday)

**Session 3**

9:20 - 10:00	<b>Shiu-Wu Chau (National Taiwan University, Taiwan, R.O.C.)</b> <i>Invited Lecture</i> Wake Modeling of Wind Turbine Array in an Offshore Wind Farm
10:00 - 10:30	<b>Yang Huang, Decheng Wan (Shanghai Jiao Tong University, China)</b> FOWT -UALM-SJTU Solver for Coupled Aero-hydrodynamic Interactions of OC3 Floating Offshore Wind Turbine
10:30 - 11:00	<b>Yi Zhang, Bin Teng (Dalian University of Technology, China)</b> High-Frequency Wave Loads and Ringing of Offshore Structures
11:00 - 11:30	<b>Dief Tarek (Kyushu University)</b> System Identification and Control Design for Kite Power System
11:30 - 12:00	<b>Di Deng, Decheng Wan (Shanghai Jiao Tong University, China)</b> Numerical Study of Vortex-Induced Motions of a Semi-Submersible Platform in Different Reduced Velocities and Current Headings
12:00 - 12:30	<b>Hongzhong Zhu (Kyushu University)</b> Modelling and Attitude Control of a Shrouded Floating Offshore Wind Turbine with Hinged Structure
12:30 - 12:40	<b>Closing Address</b> <span style="float: right;"><b>Changhong Hu</b></span>

## 国際化推進共同研究概要

### No. 17

タイトル： Step dynamics on surfaces/interfaces of a crystal: atomic and mesoscopic scales

研究代表者： Theodore L. Einstein

(Department of Physics, University of Maryland, USA)

所内世話人： 寒川義裕

実施期間： 2017年10月19日～11月2日

デバイス品質の半導体薄膜を得るにはエピタキシャル成長表面における成長素過程、特にステップダイナミクスを理解することが重要である。本研究課題では、先ず、最近の研究成果およびこの研究分野の世界動向をセミナー形式で発表し議論を行った。セミナー発表の内容を次頁に記す。次に、共同研究者を含めて集中的な議論を行った。ステップダイナミクスに関する知識を深めるとともに、引き続き共同研究を継続していくことを確認した。

Controlling step dynamics is an important ingredient to fabricate nano-scale structures on a substrate to develop new types of devices to solve energy problems. We study the step dynamics associated with the step meandering and the macrostep formation connected to dynamic phenomena on a crystal surface at the atomic scale. It is shown that the spatial periodicity of the step meandering depends on the strength of the next-nearest-neighbor (NNN) interaction between unit constituents. The attractive step-step interaction between NNN sites is shown to cause self-assembly of macrosteps at low temperatures. The origin of these NNN interactions is also studied by first-principles calculations at the atomic scale.

# **How General Ideas in Statistical Physics Helps One Understand Behavior of an Enormous Range of Systems**

Theodore L. Einstein  
(University of Maryland, USA)

While important for catalysis and growth of devices, steps on crystal surfaces also have fascinating theoretical properties based on the analogy between their two-dimensional configurations and the world lines (time evolution) of hard particles in one dimension. An adequate accounting of the distribution of the step separations (the crystal's terrace widths) can be obtained from a simple Schroedinger equation; a much better approximation is based on profound ideas about universal behavior of fluctuations. There is similar behavior in the early growth of islands on surfaces. Analogies of this nanoscale behavior are also seen in our daily lives, at over 10 orders of magnitude larger scale. Examples include times between buses in some Mexican cities, distributions of areas around subway stations, areas of districts (Japanese gun), and spacings between parked cars or birds on a wire.

## 国際化推進共同研究概要

No.18

タイトル: Water mass modification in the Japan Sea and East Asian marginal seas

研究代表者: SHIN, Hong-Ryeol

所内世話人: 千手 智晴

概要: 東アジア縁辺海の典型例として日本海を選び、深海での流れと海洋構造の長期的な変化を研究している。本年度は長崎大学の練習船「長崎丸」に乗船し、日本海南東部の大和海盆南縁において深海測流と海水特性の観測を行った。その結果、2010年に同地点で観測した結果と比べて、深層での水温が上昇していることが確認されたが、流れに関しては大きな変化は認められなかった。

# Water mass modification in the Japan Sea and East Asian marginal seas

Hong-Ryeol Shin (Kongju National University)  
Tomoharu Senju (RIAM, Kyushu University)

## Introduction

Water mass modification associated with global warming and climate change has been reported from the East Asian marginal seas, such as the Okhotsk Sea, the Japan/East Sea, the East China Sea, and the Yellow Sea. In this study, we studied the Japan/East Sea as a typical East Asian marginal sea showing long-term trends of warming and decreasing concentration of dissolved oxygen in the abyssal layer. The warming of deep waters indicates a structural change of the Japan/East Sea. However, relationship between the observed changes in the water mass structure and flow condition in the deep layer is unknown. Therefore, we carried out deep flow observations and hydrographic observations in the southern part of the Japan/East Sea.

## Observations

The direct current observations using moored acoustic current meters of RIAM, Kyushu University were carried out at the southern edge of the Yamato Basin, the southeastern Japan/East Sea (Fig. 1). The mooring operations were conducted by T/V Nagasaki Maru of Nagasaki University in May and October, 2016. Hydrographic observations with CTD were also carried out in the same cruise. These current meters were recovered on May 10, 2017 using T/V Nagasaki Maru.

## Results and Discussion

The stick diagrams of flows at Sta. Y (37°21'N, 135°40'E) are shown in Fig. 2. In addition to the mooring observation in this study, two times deep flow observations were carried out at this station in the depth range of 1800-1900 m: during the periods from May 2009 to May 2010 and from May 2010 to May 2011. Although, unfortunately, the record of current meter in this study was stopped in January 2017 due to instrument trouble, our current meter successfully captured general features in the flow field, for example, prevailing eastward flow along the isobaths and several-days fluctuation in flow speed and direction.

We here focus on the mean flows over the observation periods to investigate the long-term variation in the deep flow field. The direction and speed of mean flows are ENE (100-110°T) and about  $5.6 \text{ cm s}^{-1}$ , respectively, in the all observations (Table 1). Furthermore, standard deviations in each flow component are almost the same among the observations. This indicates that the condition of mean flows in this area is nearly same between the periods of 2009-2011 and 2016-2017, though the warming of deep water in the Yamato Basin is confirmed by some hydrographic observations.

In the eastern Japan Basin, the northern Japan/East Sea, a significant change in the mean flow is reported (Senju, personal communication). To clarify the relationship between the long-term changes in flow field and oceanic structure, we need more detailed observations.

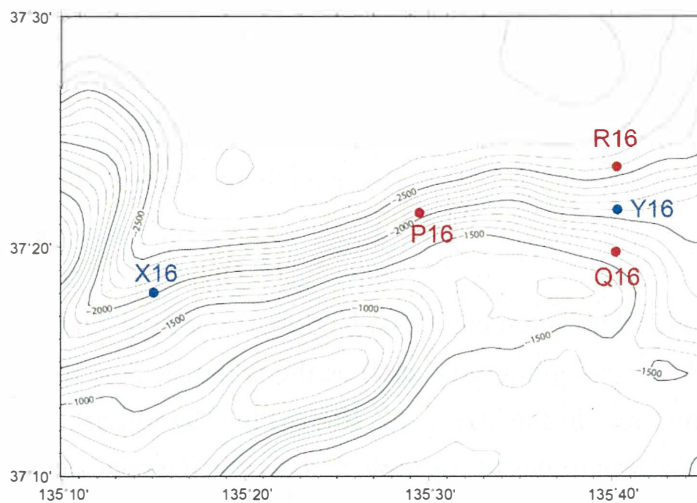


Fig. 1 Map of observation site in 2016

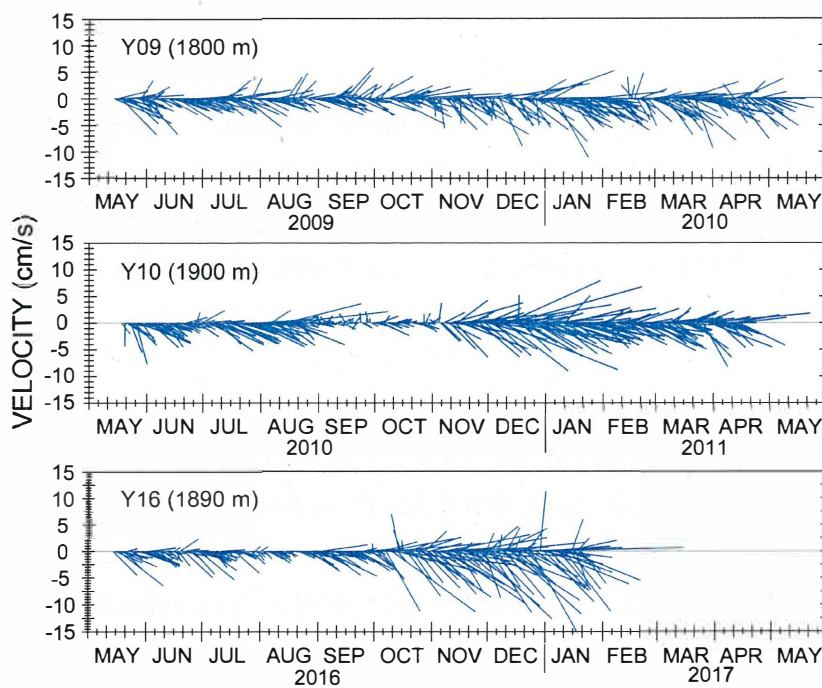


Fig. 2 Stick diagrams of flows at Sta. Y.

Table 1 Direction and speed of mean flows and standard deviations of each component

Period	Mean ( $\text{cm s}^{-1}$ )				SD ( $\text{cm s}^{-1}$ )	
	Dir. ( $^{\circ}\text{T}$ )	Speed	E-W	N-S	E-W	N-S
Y09 (1800m)	106.4	5.63	5.40	-1.59	3.55	2.55
Y10 (1900 m)	102.2	5.65	5.52	-1.20	4.44	2.45
Y16 (1890 m)	110.9	5.62	5.25	-2.01	4.39	3.45

## 国際化推進共同研究概要

No. 19

タイトル： Model inter-comparison study of long-range chemical transport model to have a better understanding of P M2.5 issue over East Asia

研究代表者： Zifa WANG

所内世話人： 鶴野 伊津志

実施期間： 2017年11月3日～11月8日、2018年3月13日～3月14日、

概要：

2015年3月末から4月初めに北京市内で観測された黄砂と大気汚染粒子の混合状態の観測結果と、同期間を対象としたモデル解析結果を Nature Scientific Report に論文として発表した。

中国華北平原から北京にかけて観測される高濃度の P M2.5 汚染とその越境影響について、野外観測結果の解析と複数の化学輸送モデルを用いた相互比較実験の取りまとめを進め、2018年3月13日～3月14日にアジア大気汚染研究センター（新潟市）と共同で、日本・中国・韓国・アメリカ合衆国・ベトナム・タイなどからの約50名の研究者が参加する MICS - Asia モデル相互比較国際ワークショップを九州大学筑紫キャンパスで開催する。

No. 19

タイトル： Model inter-comparison study of long-range chemical transport model to have a better understanding of PM2.5 issue over East Asia

研究代表者： Zifa WANG (中国科学院大気物理研究所)

### 共同研究の目的

本共同研究では、中国華北平原から北京にかけて観測される高濃度の PM2.5 汚染とその韓国・日本域への越境影響について、野外観測結果の解析と複数の化学輸送モデル (NAQPMS, CMAQ, GEOS-CHEM など) を用いた相互比較実験を進めている。

中国と福岡での最新のエアロゾルの観測装置、ライダーなどを駆使したデータの蓄積を独自に行い、同時に、中国・韓国・台湾・日本・アメリカ合衆国の研究者が進めているアジア域の化学輸送モデル相互比較実験 (MICS-Asia) への参画を通じて、PM2.5 大気汚染のモデルの問題点とその改良を進め、化学輸送モデルの精緻化を目指す。

### 共同研究の成果

今年度の PM2.5 の観測は、中国大気物研究の 325m の観測鉄塔周辺と九州大学応用力学研究所で同一の観測測値 (偏光式光学粒子計測器 POCP、化学成分連続自動分析装置 ACSA) を進めている。この観測データは、中国大気物理研究所の化学輸送モデル NAQPMS と、九大で進めている CMAQ 及び GEOS CHEM 化学輸送モデルの相互比較実験に用いることと、それを用いた中国からの研究代表者の訪日時にモデル相互比較実験の仕様の詳細を議論した。これらの成果は、2018 年 3 月 13 日～3 月 14 日にアジア大気汚染研究センター (新潟市) と共同で、日本・中国・韓国・アメリカ合衆国・ベトナム・タイなどからの約 50 名の研究者が参加し開催する MICS - Asia モデル相互比較の国際ワークショップ (九州大学筑紫キャンパス) で議論されることになっている。

## 国際化推進共同研究概要

No.20

タイトル: High resolution modeling of ocean current energy in the Tokara Strait

研究代表者: WANG, Bin

所内世話人: 広瀬 直毅

概要:

# Effects of tidal manipulation on the Kuroshio in the Tokara Strait

Bin Wang, College of Oceanography, Hohai University, China

## 1. Introduction

Numerical models have suggested that the propagation speed of the  $M_2$  baroclinic tide is 3.5-4.5m/s around the Ryukyu island chain, which is the same order of the KC (0.75-1.5m/s). The advection effect of KC, which is not represented in the early studies, is considered to be important particularly around the TK where the propagation direction of the baroclinic tide is nearly parallel to the KC path (*Niwa and Hibiya, 2004*). To examine the incoherent of the baroclinic tide, *Varlamov et al. (2015)* used a tide-resolving ocean general circulation model, and suggested that the modulation of the baroclinic tide in TS is mainly affected by the Kuroshio path variation together with the seasonal variation of the shallow thermocline. The lower-frequency ocean circulation affects the internal tides has been investigated briefly. The main purpose of this study is to clarify the effects of tides on the KC in the TS at a high resolution.

## 2. Model Configuration and Data

An extremely high-resolution regional circulation model based on the Research Institute for Applied Mechanics (Kyushu University) Ocean Model (RIAMOM) is adapted to the TS, named DREAMS\_Tokara. The model covers the TS region with the horizontal resolution of  $1/180^\circ$  longitude by  $1/225^\circ$  latitude and 33 layers in vertical. The model topography is averaged from the JTOPO30 (~1km) and J-EGG500 (Japan Expert Grid for Geography 500m). The initial and boundary conditions are determined by the simulated results of the  $1/60^\circ \times 1/75^\circ$  southwest of Japan model (DREAMS\_Energy) (*Liu et al., 2017*). To introduce the tidal effects, hourly output data of DREAMS\_Energy, which includes the tidal components, have been used to represent the tidal propagations and background currents. The other conditions of this model follow the configuration of DREAMS\_Energy. The model is integrated for more than 3.5 years, and the analyzed period is from 1 January 2012 to 30 September 2015. The moving vessel ADCP data and CTD data along the ferry line between Kagoshima and Naha provided by the Kagoshima University Faculty of Fisheries are used to validate the simulated results.

### 3. Results

The simulated results are in good agreement with hydrographic observations. Compared to the model without tides, the occurrence of the internal tides and corresponding changes in the density fields are found in the downstream of the Tokara Strait. The main axis of the Kuroshio in the model with tides moves to the south slightly at the eastern part of the Tokara Strait. Furthermore, there is concentration of the stronger current (magnitude of current speed  $> 60$  cm/s) to the upper layer. The vertical shear of the current becomes larger and the Kuroshio becomes more baroclinic. Nevertheless, the detailed mechanism for this nonlinear interactions between the Kuroshio Current and the internal waves must await further investigation.

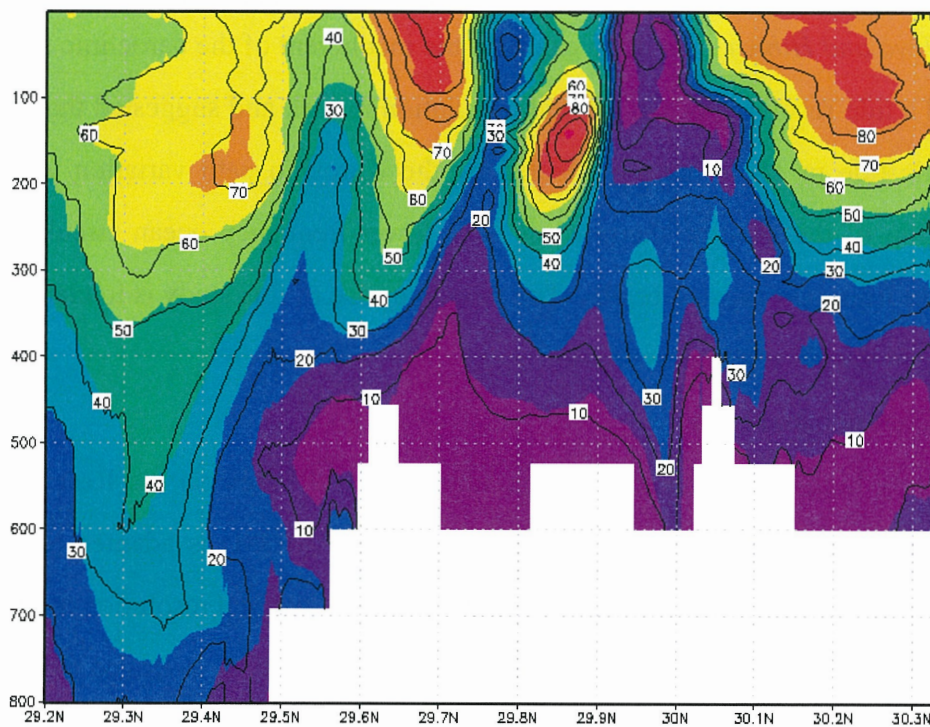


Fig 1. Magnitudes of the simulated Kuroshio Current in August along  $130^{\circ}\text{E}$  for the tidal simulation (color map) and non-tidal simulation (contours).

### Acknowledgments

This work was supported in part by the Collaborative Research Program of Research Institute for Applied Mechanics, Kyushu University.

## 国際化推進共同研究概要

No.21

タイトル: Dynamical mechanisms of stratospheric control on the tropical troposphere and ocean

研究代表者: Ueyama, Rei

所内世話人: 江口 菜穂

概要: 1990年代後半から現在における熱帯の大循環場の変化を気象データ(人工衛星、客観解析等)を用いて解析を行った。特にここ30年間で北半球夏季に南東太平洋の水温の低下がみられ、それは赤道をまたぐ南西風の強化、すなわち対流圏内の南北循環場(Hadley循環;HD循環)が北側へシフトしたことに起因することがわかった。さらにHD循環の強化が、近年の温室効果気体の増加による成層圏の寒冷化によって変調をきたした成層圏の南北循環場(Brewer-Dobson循環)と関係することが示唆された。

# Dynamical Mechanisms of Stratospheric Control on the Tropical Troposphere and Ocean

Rei Ueyama (NASA Ames Research Center)

## I. Abstract

The cause of recent (from the mid to late 1990s) decadal variations in tropical circulation is studied by making use of a meteorological reanalysis dataset. Cooling of the equatorial southeastern Pacific Ocean occurred in association with enhanced cross-equatorial southerlies, which resulted from a strengthening and poleward shift of the rising branch of the boreal summer Hadley circulation connected to the stratospheric Brewer–Dobson circulation. From boreal summer to winter, the anomalous convective activity center moves southward following the seasonal march to the equatorial Indian Ocean–Maritime Continent region, which strengthens the surface easterlies over the equatorial central Pacific. Accordingly, ocean surface cooling extends over the equatorial central Pacific. We hypothesize that the fundamental factor causing the recent decadal change in the tropical troposphere and the ocean is a poleward shift of the rising branch of the summertime Hadley cell, which can result from a strengthening of extreme deep convection penetrating into the tropical tropopause layer (TTL), in particular over the continents of Africa and Asia, and adjacent oceans. We conjecture that this effect is produced by a combination of land surface warming due to increased CO<sub>2</sub> and a reduction of static stability in the tropical tropopause layer due to tropical stratospheric cooling.

## II. Introduction

Large changes in tropical circulation occurred from the mid to late 1990s. These include (i) a slowdown, or hiatus, of global warming in association with a decrease in the tropical eastern Pacific sea surface temperature (SST), (ii) the advancement of the onset of the Asian summer monsoon, and (iii) an increase in precipitation in western Africa over the Sahel and in southern Africa during the austral summer. Besides the large-scale circulation changes, mesoscale phenomena such as an increase in the cyclone frequency and intensity over the Arabian Sea were also reported. Wang et al. (2012) argued that these phenomena are related to the early onset of the Asian summer monsoon. Several studies have also shown a relationship between changes in the TTL and the tropical troposphere, namely tropical cyclone activity in the Atlantic (Emanuel et al., 2013) and the intensity of tropical storms and SSTs (Ramsay, 2013; Wang et al., 2014).

## III. Method/Data

Datasets used in this study include JRA55 reanalysis, JRA55-AMIP (which uses the same model and boundary conditions as JRA55, but without assimilation of observational data in the atmosphere), outgoing longwave radiation derived from High Resolution Infrared Radiation Sounder, Global Precipitation Climatology Project precipitation, and COBE-1 gridded SST.

## IV. Results

Since the mid 1990s, equatorial ocean in the southern hemisphere has cooled in association with a strengthening of cross-equatorial southerlies near the surface. This was induced by a northward shift of convective activity connected to the rising branch of the Hadley circulation and the stratospheric Brewer–Dobson circulation. Water vapor transport by the enhanced cross-equatorial southerlies further amplified the convective activity in the northern hemisphere. An increase in the vertical velocity was most apparent

in the TTL, which may have been driven by the decreased stability in the TTL from the combined effects of lower stratospheric cooling and upper tropospheric warming.

#### V. Discussion/Summary

We hypothesize that recent tropical circulation changes originate primarily from a strengthening of deep convective activity over the continents and their vicinity in the summer hemisphere, particularly over the African–Asian sector. This working hypothesis applies well during boreal summer and where a large land mass is located off the equator. Further investigation is needed to determine whether the stratosphere is merely passively responding to the tropospheric warming or playing an active role in the tropospheric circulation change.

To better understand the details of the stratosphere–troposphere coupling process, we will conduct case studies on the northward shift of convective activity similar to that associated with the recent trend, but associated with a sudden cooling of the tropical stratosphere during a boreal summer monsoon. The coupling process as depicted in convective overshooting and cloud top data will be the topic of future work.

#### VI. List of Publications

Kodera, K., Eguchi, N., Ueyama, R., Kuroda, Y., and Kobayashi, C.: Impact of tropical lower stratospheric cooling on deep convective activity: (I) Recent trends in tropical circulation, *Atmos. Chem. Phys. Discuss.*, <https://doi.org/10.5194/acp-2018-128>, in review, 2018.

#### VII. Research workshops and seminar

Joint SPARC Dynamics & Observations Workshop: QBOi, FISAPS & SATIO-TCS

October 9–14, 2017; Kyoto University, Kyoto, Japan

Program of the workshop, list of participants, and proceedings can be found at:

<http://www-mete.kugi.kyoto-u.ac.jp/SPARCjws2017/>

#### VIII. References

Emanuel, K., Solomon, S., Folini, D., Davis, S., and Cagnazzo, C.: Influence of tropical tropopause layer cooling on Atlantic hurricane activity, *J. Clim.*, 26, 2288–2301, <https://doi.org/10.1175/JCLI-D-12-00242.1>, 2013.

Ramsay, H.: The effects of imposed stratospheric cooling on the maximum intensity of tropical cyclones in axisymmetric radiative–convective equilibrium, *J. Clim.*, 26, 9977–9985, doi: 10.1175/JCLI-D-13-00195.1., 2013.

Wang, B., Xu, S., and Wu, L.: Intensified Arabian Sea tropical storms, *Nature* 489, E1–E2, doi:10.1038/nature11470, 2012.

Wang, S., Camargo, S.J., Sobel, A.H., and Polvani, L.M.: Impact of the tropopause temperature on the intensity of tropical cyclones—an idealized study using a mesoscale mode, *J. Atmos. Sci.*, 71, 4333–4348, 2014.

#### IX. Member

Rei Ueyama	NASA Ames Research Center
Nawo Eguchi	RIAM, Kyushu University
Kunihiko Kodera	ISEE, Nagoya University

## 国際化推進共同研究概要

No.22

タイトル: Calculation of backscatter optical properties of cirrus clouds for mixtures of ice crystals with different shapes and orientations

研究代表者: BOROVOY, ANATOLY, GEORGIEVICH

所内世話人: 岡本 創

概要: 衛星搭載ライダーと地上ライダーによる氷粒子の解析を目的として、散乱理論の基づいて氷粒子の散乱特性を調べた。

波長 355nm, 532nm, 1064nm における後方散乱係数の波長依存性を示す後方散乱カラー比、偏光解消度のカラー比、およびこれらの波長におけるライダー比と偏光解消度の関係の解析も行った。これらの値は、いずれも、明確なサイズ依存性、粒子形状依存性を示していた。

これらの共同研究の結果は、JQSRT 2016, SPIE 2017 の 2 編の論文で公表された。

No. 22. Calculation of backscatter optical properties of cirrus clouds for mixtures of ice crystals with different shapes and orientations

Institute of Atmospheric Optics, Rus. Acad. Sci., Prof. A.G. Borovoy

Aim:

Development and approbation of the methods for retrieving the microphysical characteristics of cirrus clouds from the data of the ground-based and space lidars.

Magnitude of the task is provided by the fact that a number of satellites sounded in the former time and, at present, are sounding the cirrus clouds at optical and microwave wavelengths. A number of similar satellites are also constructed now. In addition, the cirrus clouds are sounded by numerous ground-based lidar stations whose data are combined in various lidar nets. However, the accuracy of retrieving the optical and microphysical characteristics of the clouds obtained from these measurements do not correspond yet to the demands of the numerical models of the Earth radiative balance. However, accuracy of retrieving the optical characteristics from these measurements don't satisfy the demands of the numerical models for the Earth's radiative balance. Moreover, the existing methods for retrieving such microphysical characteristics from remote sensing instruments, as a rule, are not justified theoretically that often leads to inconsistent data.

Method:

The problem of light scattering by nonspherical particles is a complicated problem of the mathematical physics. The problem of light scattering by ice crystal of cirrus clouds was solved earlier in the approximation of geometric optics where the wave properties of light were ignored (ray-tracing algorithm, K.N. Liou, USA; A. Macke, Germany). In the current literature concerning the optical characteristics of cirrus clouds, the predominant role belongs to the large team of American authors where the central role plays Prof. Ping Yang. These co-author's team has a huge scientific productivity. They publish in average one paper in high-rating journals for every 1 - 2 months. In these papers, the calculation algorithm developed by Ping Yang and called as IGOM (improved geometric-optics method) is used. In this algorithm, the wave properties of light is taken into account approximately. Some modification of IGOM was made later by Masuda in Japan [ Masuda K. et al., Papers Meteorol. Geophys. v. 63, 15, 2012].

For example, Prof. Ping Yang with co-authors for several last years published three papers where the light backscattering by ice crystals was calculated by his IGOM (improved geometric-optics method) algorithm: [J. Quant. Spectrosc. Radiat. Transfer v. 79-80, 1139, 2003; J. Quant. Spectrosc. Radiat. Transfer v. 100, 91, 2006; J. Geophys. Res. v. 114, D00H008, 2009]. And only in his recent papers of 2015-2016 [ Opt. Express v. 23, 11995, 2015; Opt. Express v. 24, 620, 2016] he agreed that his algorithm IGOM is not applicable to calculate the light backscattering in cirrus clouds.

At present, the physical-optics method seems to be most acceptable for calculation of light backscattering by ice crystals of cirrus clouds. This method was proposed by us in 2003 [J. Opt. Soc. Am. v. 20A, 2071, 2003] and then it was finalized as a reliably operating computer algorithm [Borovoi A., Konoshonkin A., Kustova N., Opt. Lett, v. 38, 2881, 2013]. The advantages of this method is, first, simple physical interpretation of all computation procedures and, second, a possibility to fulfill the calculations by use of the personal computers instead of supercomputers. It is interesting to note that Prof. Ping Yang (USA) with co-authors had come to the same method only in 2011 that was published in the paper [J. Quant. Spectrosc. Radiat. Transfer v.112, 1492, 2011]. However, these authors had not refined this method to the available algorithms and they don't use this method at present, as far as we know. The reason of this was that they came to developments of two exact methods demanding to use supercomputers. The first method called PSTD is the improved FDTD method that is discussed in the papers [ 1) J.

Quant. Spectrosc. Radiat. Transfer v. 113, 1728, 2012; 2) Opt. Express v. 20, 16763, 2012; 3) J. Quant. Spectrosc. Radiat. Transfer v. 129, 169, 2013; 4) Opt. Express v. 22, 23620, 2014]. The second method is called the invariant imbedding T-matrix method (II-TM), it is described in the papers [J. Quant. Spectrosc. Radiat. Transfer v. 116, 169, 2013] и [J. Quant. Spectrosc. Radiat. Transfer v. 138, 17, 2014].

### Simulations in 2017

We used the physical-optics method for calculating the backscatter Mueller matrix and the backscatter ratios for the following input parameters:  
crystal shapes: hexagonal plates, hexagonal solid and hollow columns, solid columns with distorted shape, bullet-rosettes and droxtals;  
wavelengths: 0.355, 0.532 and 1.064 micrometers;  
crystal sizes: from 10 up to 1000 micrometers;  
crystal orientations: quasi-horizontal orientation with arbitrary effective crystal tilts up to the random orientation;  
lidar tilts: 0, 3 and 5 degrees about the vertical direction.

### Results:

We concluded that the backscatter ratios (lidar, depolarization and color ratios) reveal strong dependence on shape and size of the crystals.

### Joint publications:

1. Konoshonkin A.V., Borovoi A.G., Kustova N.V., Okamoto H., Ishimoto H., Grynko Y., Förstner J. Light scattering by ice crystals of cirrus clouds: from exact numerical methods to physical-optics approximation // Journal of Quantitative Spectroscopy and Radiative Transfer. 2017. V. 195. P. 132-140. doi: 10.1016/j.jqsrt.2016.12.024
2. Kustova N.V., Konoshonkin A.V., Borovoi A.G., Okamoto H., Sato K., Katagiri S. Power laws for the backscattering matrices in the case of lidar sensing of cirrus clouds // Proceedings of SPIE, V. 10466. [10466-116]. 2017